POLITECNICO DI TORINO

Master's Degree in Mathematical Engineering

Master's Thesis

Duplication of re-entry flight conditions in plasma wind tunnels.

von KARMAN INSTITUTE
FOR FLUID DYNAMICS

Supervisors:
Prof. Luigi Preziosi
Prof. Olivier Chazot

Candidate:
Tommaso Fedeli

A.A. 2023/2024

Ackowledgments

My heartfelt thanks go to Prof. Olivier Chazot for the opportunity to work in his research group at the Aerospace Department, to Dr. Pierre Schrooyen for his patience and clear explanations, and to my supervisor, Prof. Luigi Preziosi, for his availability and helpfulness.
Last but not least, to my family and friends, at home and abroad,

Tommaso Fedeli.

Contents

Abstract

In the framework of atmospheric re-entry, the scope of this thesis is to investigate a subsonic-hypersonic aerothermodynamic similarity for probe designing and high-enthalpy testing. After a review of the foundations of aerothermodynamics, Local Heat Transfer Simulations and high-order reactive boundary layer theory are used to build a mapping from flight conditions to ground testing facilities. A two-dimensional computational study is then performed on an axi-symmetric probe with different shapes and physical conditions with the software ARGO. The results are used to estimate the effects of these variations on the paramaters involved in the aforementioned similarity and to build a reference study for the possible flight environments replicable in the von Kárman Institute for Fluid Dynamics' Plasmatron facility. Comparison with hypersonic simulations is used at last to validate the method on a real test case.

List of Figures

List of Tables

Chapter 1

Introduction

The nature of scientists' and engineers' interest in Space exploration is two-fold: on one hand there is the timeless driving force of scientific inquisitiveness and intellectual responsibility to understand not only the world we live in, but also the universe we are surrounded by. Conversely, the global population is projected to reach 10 billion people in the coming years [56], which, along with predicted increases in CO_2 and other pollutants concentrations [2] underscores the urgent need to address several critical issues, such as the need for new resources. The situation is further exacerbated by geopolitical polarization and the deterioration of international relations, which have historically accelerated technological advancement but now pose a serious threat to the survival of the human race. In these circumstances, space exploration is likely to become more than just a curiosity.

1.1 Motivation

Re-entry is clearly amongst the most difficult challenges in rocket science and Space exploration, since it involves precise calculations aimed at guaranteeing safety from the initial stages of high speed entry into the planetary gaseous environment, to the final landing on the surface. During hypersonic flight the vehicle is subject to an extreme heat load generated by the dissipation of kinetic energy into thermal energy. In this regime engineers face a dual challenge in designing spacecrafts: configuring the geometric and material aspects to withstand the heat load throughout the mission duration, while also mitigating the risk of space debris formation. For the first purpose, Thermal Protection Systems (TPS) are essential to shield the vehicle's surface and maintain the body integrity under these severe conditions. They are usually divided in the category of ablative or reusable, depending on the specifics of the mission, such as speed and temperatures. The former exploit material

degradation to absorb the heat and are typically used in high enthalpy and high speeds re-entry, where corrosion is inevitable, such as Mars missions [1]. They consist of a polymeric resin that decomposes into gas first through pyrolisis and carries heat out of the TPS. Mass efficiency can be managed with new lightweight materials, but careful consideration has to be given to the induced roughness, which could impact boundary layer transition. Under less extreme conditions the latter are instead preferred, but are limited to Low Earth Orbit (LEO) flight, where velocities don't exceed $8 - 10$ km/s [57]. They mainly consist of passiveley cooled structures that don't effect payload as much and can be used for multiple missions. To ensure that vital components can withstand the flight environment, the heat load must be carefully evaluated during the design phase. This evaluation determines both the necessary properties of the material and the required thickness of the shield. The lack of a proper understanding of re-entry physics usually leads to overly conservative safety coefficients, which could impact mass load, maeuverability and overall costs that can have catastrophic consequences on the missions. Many incidents were registered in recent years, such as ESA's ExoMars mission [54]. Even successful missions paid the price on the lack of a robust theoretical and experimental basis, such as ESA's IXV and Galileo probes, both of which reached dangerous levels of ablation downstream with a heavily overestimated TPS thickness at the nose.
The second issue arises because materials used in spacecraft construction, when exposed to aerodynamic forces, may degrade and fragment into smaller pieces. These fragments may follow different trajectories from the main body and are thus not guaranteed to fully disintegrate during re-entry. This presence of Space debris is concerning as it poses potential hazards to other spacecraft and future missions. In 2021, during the re-entry of a SpaceX Falcon 9 rocket's second stage, debris from the rocket entered the Earth's atmosphere and caused a fireball over the Pacific Northwest. This incident highlighted concerns over the safe disposal of rocket stages and the potential risk of debris causing damage upon re-entry. Since the Apollo XI mission in 1969, many advancements in Space exploration and re-entry physics have been made, as evidenced by several successful manned and unmanned missions. However, the path towards a comprehensive understanding of these phenomena remains an extremely complex task even for newer probes.

1.2 Re-entry challenges

Estimating the effects of the flight environment is notoriously difficult: precise calculations of the high temperature environment on the materials involved are influenced by different contributions.

Firstly, the range of altitudes involved in the entire trajectory is so vast that changes in density, pressure, and temperature must be considered, as shown in Figure 1.1. This complexity increases when taking into account the inevitable Space debris generated during operations. As already outlined, spacecraft and capsules can break into several pieces with different geometries, each following distinct paths during re-entry. Consequently, they will encounter varying external conditions, which could determine whether they burn up or survive the flight.

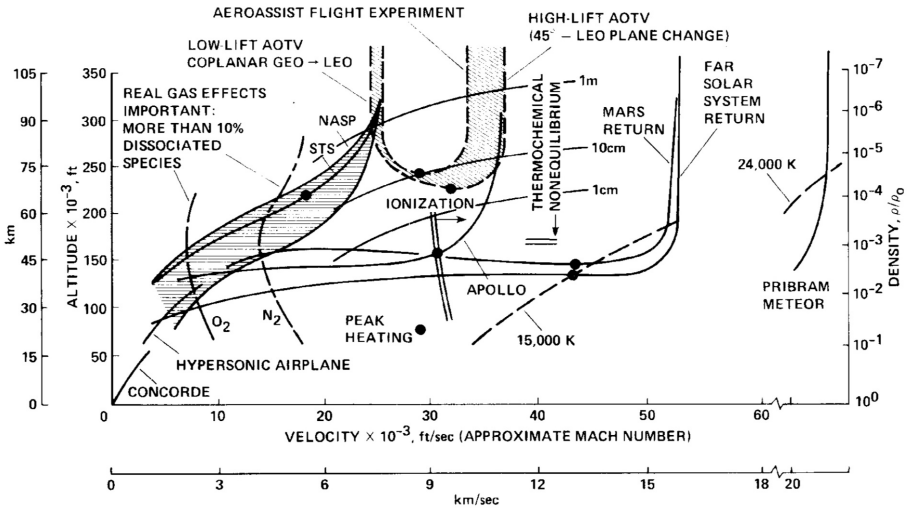

Figure 1.1: Trajectory physics, from [33].

In addition chemical reactions between species, high temperature effects [4], and other phenomena such as rarefaction, gas-surface interaction, radiative and plasma effects, play a significant role, affecting maneuverability and material integrity, with the air surrounding the vehicle reaching more than 10000 K. For this reason, in hypersonic flows, bodies must be blunted to reduce heat transfer at the nose and facilitate internal heat conduction. This geometric configuration leads to the formation of detached shock waves ahead of the body, which compress molecules and transfer energy to different internal gas modes at varying rates, often leading to a state of thermal non-equilibrium. Shock waves also influence chemical reactions, causing dissociation of molecules and atomic ionization. Species typically do not have sufficient time to reach equilibrium composition before recombining at the wall, resulting in an unstable mixture. A schematic representation of high temperature effects on air chemistry can be seen in Figure 1.2.

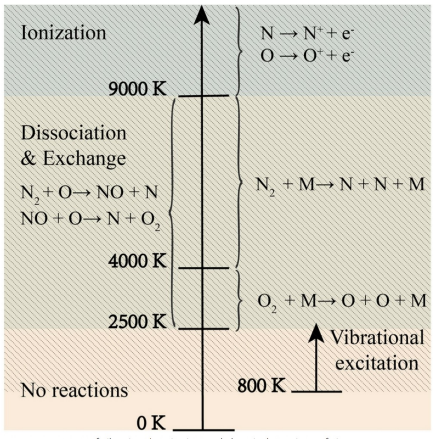

Figure 1.2: High temperature effects on chemical species, from [58].

Furthermore, vehicle geometry can impact the nature of the flow behind the capsule. Flow separation can occur due to strong backward facing steps downstream, penalizing maneuverability, while boundary layer transition can drastically increase drag. Consequently, most of the designing process typically relies on empirical or semi-epirical data, which often leads to extremely conservative approaches, negatively impacting budget, but also performance and stability. A summary of hypersonic flight conditions can be seen in Figure 1.3.

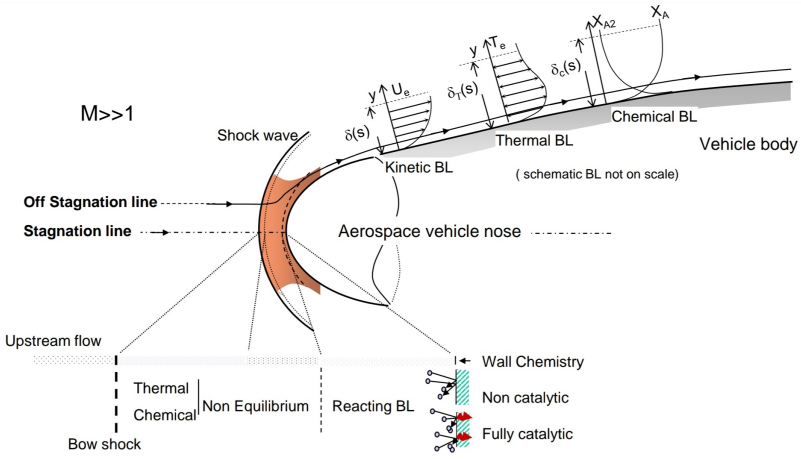

Figure 1.3: Aerothermodynamics environment around a blunt body, from [19].

More comprehensive studies are thus needed, including alternative treatments for one or more of the effects. Although experimental tests remain a primary source of data for understanding how vehicles operate during re-entry, they are limited for several reasons.

1.3 Plasma wind tunnels

Conducting precise flight experiments to assess the material response of hypersonic re-entry vehicles can be extremely difficult. In-flight measurements can become economically and technically demanding, necessitating sophisticated tools and sensors. Furthermore, they are impractical for design purposes and predicting Space debris formation and burning. Ground tests are, on the other hand, heavily limited in reproducing those extreme conditions, due to high uncertainties and small test times. Nowadays several wind tunnels are used around the globe to study a specific aspect of the probe, ranging from hypersonic cold tunnels for preliminary design studies to Arc Jets and Inductively Coupled Plasma (ICP) facilites for high temperature testing.
Arc-jets operate by creating a discharge between two electrodes, generating a high enthalpy dissociated flow, which is then accelerated to supersonic speeds with a converging-diverging nozzle. These facilities can operate at higher enthalpies and velocities, and can sustain large test models, but electrode contamination of the flow due to nonequilibrium conditions can complicate the assessment of the testing conditions.
The ICP system starts with a high frequency and high voltage generator. This generator creates an alternating current that flows through a coil surrounding a quartz tube. The current in the coil induces circular oscillating electric fields perpendicular to the axis of the quartz tube, where low pressure Argon[1] is introduced to initiate an electric discharge. The movement of free electrons creates a secondary current within the quartz tube which heats the argon gas through the Joule effect. The jet is then introduced into the chamber, where the sample is held in place. These facilities have been developed since the 1950s and are still preferred for their performance and ability to create purer plasmas and thus precisely emulate the high enthalpy environments experienced during flight. Several ICP tunnels are in use in Europe, such as PHEDRA in Orléans and Plasmatron at the von Kárman Institute for Fluid Dynamics in Sint-Genesius-Rode (Belgium), developed in 1992 as a collaboration between the European Space Agency (ESA) and European national Space programs, originally intended to fit the Hermes vehicle flight conditions. The facility uses a $(1.2\ MW, 400\ kHz, 2\ kV)$ solid state generator that can provide a uniquely wide testing conditions envelope, with enthalpies in the range $[5, 60]\ MJ/kg$ and pressures in the interval $[1, 22]\ kPa$. More details on the facility can be found in [16]. A test is visible in Figure 1.4.

[1] a gas where free electroncs have a long lifetime

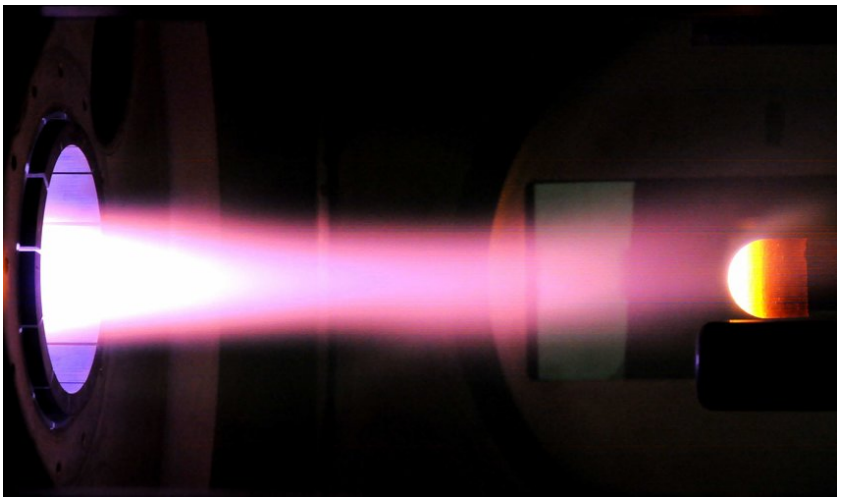

Figure 1.4: A test at the Von Kárman Institute Plasmatron facility.

These facilities are crucial for TPSs design and vehicle components analysis. Advancements on this front could potentially lead the way to develop more robust and reliable capsules, but special attention has to be given to the physical conditions inside the test chamber to reproduce an environmnent sufficiently close to the real flight conditions in order to leverage ground test data. To this day facilities that can reach high Mach number such as Arc Jets don't have enough testing time to reproduce the thermal exchange properly. Therefore only partial ground reproduction can be achieved. On the other hand, ICP facilities excel at sustaining dissociated flows over extended periods, aimed at faithfully replicating aerothermochemical environments, but they cannot attain high speeds or accommodate large test probes. As a result, fully accurate and comprehensive replication of re-entry flight conditions is unattainable, limiting the focus to a restricted number of coupled effects at any given time.

Local Heat Transfer Simulation

A further challenge in ground testing arises from the interaction between the intrinsic nature of reactive flows and the geometric scaling of the problem. Research has shown [48] that achieving a complete replication of the hypersonic environment is unfeasible without employing a full-scale model of the component. This necessity compels engineers to develop methods for extrapolating between ground-based and flight-based conditions. Such extrapolation methods are essential even when testing small full-scale components because the selected facility may not be able to replicate the flight conditions accurately. A possible solution to overcome this complication is to restrict the analysis to the stagnation point region as suggested initially by the works of Fay and

Riddel [25] and Rose and Stark [50] and later fully developed by Kolesnikov [37]. This theory, called Local Heat Transfer Simulation (LHTS), effectively describes the entire boundary layer of the vehicle based on three physical parameters of the flow, which by themselves determine the stagnation point heat load-the most critical for shields and vehicle parts-independently of the flow regime. Several articles have been published to validate the theory on non-ablative resusable TPMs [8], including other effects such as mass blowing [3], but to this day now there has not been a comprehensve reference study that includes both geometric and physical effects on the parameters involved in the LHTS similarity. The necessity of including both effects is two-fold. As already mentioned, different shapes will follow different trajectories and experience different conditions. Various geometries not only naturally emerge from debris formation, but also heavily influence the nature of the flow, possibly inducing turbulent transition and flow separation. Moreover, the geometric parameters are actively involved, alongside the physical conditions, in the extrapolation procedure that links the subsonic conditions to a real flight environment. A detailed analysis will be given in section 2.4. Therefore including a large range of possible experimental setups is aimed at fully characterizing the flight conditions that can be studied with a particular facility, accounting for different trajectories and components.

1.4 Computational Fluid Dynamics

Computational Fluid Dynamics (CFD) provides both a preliminary and complementary tool for test engineers, as it helps optimize testing conditions and designs. Researchers can use CFD to identify and address potential issues early in the design process, reducing the need for costly and time-consuming physical tests, which are not only economically expensive, but also complex to set up. Understanding the general behavior of the flow is an extremly useful step in order to later interpret the tests results. For this reason, as a preliminary tool, numerical invstigations can be employed to perform parameter sensitivity analysis and how they affect the heat load and the flow structures. CFD can also be used for both comparison and predictions, as it is not constrained by mechanical sources, generators, measuring instruments, or sensors. This allows for extended studies without the need for technological advancements and without any safety concerns.
While hypersonic simulations offer the most accurate reproduction of flight conditions, their implementation presents significant challenges. In contrast, subsonic simulations can serve both as surrogate for ground tests and as precursors to a more comprehensive software, focusing specifically on flight conditions following strong shocks.

While CFD certainly is a great tool to study these effects, a robust numerical approach for high temperature gases needs to include the aforementioned phenomenological observations to increase the fidelity of the simulation, without compromising computational times and costs. Consequently it is still crucial to simplify the model to best fit the working conditions of the facility. The same argument applies to the simulation setup, where a tradeoff between accuracy, robustness and efficiency is essential.

1.5 Aim of the thesis

Hypersonic flight remains a complex topic to properly model due to several factors. Fully reproducing those extreme conditions on the ground is not only currently impossible, with each facility focusing on few effects at a time, but is also limited by the necessity to use scaled models. As a result, spacecraft design is extremely challenging, especially since thermal shields must ensure the capsule integrity throughout the mission without significantly impacting the payload, while other components are expected to fully burn upon re-entry. Preliminary studies still rely on the limited empirical data available, leading engineers to choose exceptionally conservative safety factors despite their disadvantages. To leverage some information from plasma wind tunnel testing ground-to-flight extrapolation methods establish a canonical mapping between subsonic and hypersonic stagnation point heat loads, which are critical for estimating TPS thickness and Space debris formation based on wind tunnel experiments. The ultimate goal of this thesis is to understand how probe geometries and experimental conditions can influence the parameters involved in the duplication, in order to highlight the possible flight environments the facility can reproduce. In particular, the project aims to provide a solid foundation for the design of test probes by analyzing the subsonic flow produced by various shapes in the range of the von Kárman Institute Plasmatron physical conditions. To achieve this, a number of two-dimensional subsonic high temperature DNS (Direct Numerical Simulation) simulations will be conducted with the software ARGO, developed at Cenaero. Each simulation will be used to estimate the relevant parameters, allowing the construction of an envelope that will characterize the facility. The effect of varying test conditions on these parameters will be treated individually to determine each one's contribution.
The thesis is organized as follows: in Chapter 2 the mathematical and physical frameworks of reactive flows are developed from the basics of compressible flow, adding the necessary theory step by step, from mixture thermodynamics, high temperature effects for low Reynold numbers, to LHTS theory and reactive boundary layers. A brief description of the software ARGO, with some notions of Discontinuous Galerkin methods are presented in Chapter 3. In Chapter

4 some preliminaries on the computational setup will be followed by a series of simulations used to extrapolate stagnation line characteristic parameters around a two-dimensional axisymmetric test probe. Finally, an hypersonic simulation is used to evaluate the extrapolation procedure effectivness.

Chapter 2

Physics of reactive flows

This chapter provides an introduction to the physical modeling of reactive compressible flows. The primary areas of focus will include the thermodynamics, kinetics, and transport properties of the mixture. Special attention will then be given reactive boundary layers and their self-similar analysis. A summary of local heat transfer simulation will follow, providing insights into how heat transfer phenomena can be used as a bridge between hypersonic flight and subsonic tests. To achieve the duplication of the conditions, boundary layers analysis at low Reynolds numbers will be presented, highlighting the unique characteristics and challenges associated with these conditions.

2.1 Fundamentals of gas dynamics

The most fundamental theory of gases is kinetic theory, with the Boltzmann equation as the main governing balance law. Different assumptions can be made on this equation to derive simplified models of reality. For gas dynamics the most important one is the continuum hypothesis. The kinetic approach is govered by the Knudsen number $Kn = l/L$ which compares the particles free-mean path l and the characteristic scale of the problem L. When collisions happen frequently enough it is reasonable to assume the gas will occupy all the volume available. Different regimes of Kn lead to different balance equations, from Euler and Navier-Stokes to the more complex Burnett system [51]. Since the latter are notoriously difficult to solve and have shown stability issues, in transition regimes adjustments are made to employ the more common Navier-Stokes system. Rarefaction effects become significant in hypersonic flow under conditions of low density, such as during missions from distant planets in the solar system, or at high altitudes during re-entry. For instance, the aerodynamics of the Space Shuttle cannot be accurately described using fully continuum theory above an altitude of 92 km [4]. However, since the primary focus of this

thesis is the Plasmatron facility, the continuum hypothesis will be employed. The starting point of this analysis will then be the balance laws of continuum mechanics in a cartesian reference frame for a mixture composed by N_s species. The system, for sufficiently regular solutions, can be written as

$$\begin{aligned} \frac{\partial \rho_i}{\partial t} + \nabla \cdot (\rho_i \mathbf{u}_i) &= \dot{\omega}_i \quad \forall i = 1, .., N_s \\ \frac{\partial (\rho \mathbf{u})}{\partial t} + \nabla \cdot (\rho \mathbf{u} \otimes \mathbf{u}) &= \nabla \cdot \boldsymbol{\sigma} + \rho \mathbf{f} \\ \frac{\partial (\rho E)}{\partial t} + \nabla \cdot (\rho E \mathbf{u}) &= -\nabla \cdot \mathbf{q} + \boldsymbol{\sigma} : \mathbf{D} + \dot{\omega}_T, \end{aligned} \tag{2.1}$$

The first equations are balance of the N_s species density, while the remaining are respctively mixture momentum and mixture energy balance. In this system ρ_i is the species density, $\mathbf{u}_i$ the species velocity, while ρ and $\mathbf{u}$ are mixture density and mixture velocity, $E = e + \frac{1}{2}\|\mathbf{u}\|^2$ is the mixture total internal energy, which is the sum of specific internal energy and kinetic energy, $\mathbf{q}$ is the heat flux, while $\boldsymbol{\sigma}$ is the mixture stress tensor contracted with the strain-rate tensor $\mathbf{D} = \frac{1}{2}\nabla \mathbf{u} + (\nabla \mathbf{u})^T)$. Finally, $\dot{\omega}_i$, $\rho \mathbf{f}$ and $\dot{\omega}_T$ represent species mass, mixture momentum, and mixture energy source terms. This system needs closure with choosing constitutive laws for $\boldsymbol{\sigma}(\mathbf{D})$, $\mathbf{q}(T, \nabla T)$, together with an equation of state $p(\rho, T)$. For instance, a compressible viscous fluid, which obeys Fourier law of conduction and the perfect gas equation of state, satisfies:

$$\begin{aligned} \boldsymbol{\sigma} &= -p\mathbb{1} + \boldsymbol{\tau} = (-p + \lambda \operatorname{tr}(\mathbf{D}))\mathbb{1} + 2\mu \mathbf{D} \\ \mathbf{q} &= -\kappa \nabla T \\ p &= \rho R T, \end{aligned} \tag{2.2}$$

where p is the mixture thermodynamic pressure, T is the temperature, while λ and μ are respectively second and shear viscosity coefficients and κ is the thermal conductivity.

The scope of the following section is to justify the system (2.1), introducing the necessary tools to describe species and mixture thermodynamics and their interconnections, chemical reactions, heat and mass transfer phenomena, highlighting the limitations of Fourier law and the assumption of calorically perfect gases. Finally, the derivation of the system (2.1) will be briefly discussed along with a summary of the balance laws employed in the numerical study. A comprehensive treatment of aerothermodynamics would require extensive knowledge of quantum statistical mechanics and kinetic theory to rigorously derive an analytical model based on first principles. However, since this is not the main topic of this thesis, the theoretical foundations will not be covered. Since the scope of the present work is to investigate simple model to provide

a basis for future experimental tests, a non-ablative cooled probe will be assumed, ensuring that radiative heat transfer does not affect the surface energy balance. Similarly, electromagnetic interactions can be neglected if the sample is held far enough from the ICP torch, where the flow is ionized before entering the test chamber.

Nondimensionalization

To identify the similarity between different flows, nondimensionalization is a standard procedure in fluid mechanics. For this purpose, some of the most important nondimensional parameters involved in this analysis are listed in Table 2.1, where U is a characteristic velocity of the flow, c is the speed of sound and c_p is the specific heat at constant pressure.

Number	**Symbol**	**Measure**	**Expression**
Knudsen	Kn	Continuum hypothesis	l/L
Mach	Ma	Compressibility	U/c
Reynolds	Re	Convection-diffusion ratio	$\frac{\rho U L}{\mu}$
Prandtl	Pr	Viscosity-conductivity ratio	$\frac{c_p \mu}{\kappa}$

Table 2.1: Nondimensional numbers for system (2.1).

The necessity to include new phenomena in this framework will results in the definition of new nondimensional numbers.

2.2 Nonequilibrium flows

In classical fluid mechanics, one energy parameter is typically sufficient to describe the state of a gas. However, in reality, dilute mixtures consist of individual particles that interact minimally with each other but possess energy stored in various forms: translation, rotation, vibration, and electronic excitation.
At lower temperatures, molecular energy primarily exists in the form of translation and rotation. As temperature increases, molecules begin to vibrate, eventually leading to dissociation into atomic species. At even higher temperatures, electrons, initially occupying only their ground state, can become excited, weakening their bond with the atom and potentially causing ionization as temperatures rise further. These different energy modes can interact and relax over different timescales. By the time sufficient molecular collisions have occurred and a new stable thermodynamic equilibrium is established, the fluid element of interest has typically moved downstream. Therefore, to fully

characterize the thermal state of the system in such conditions, multiple energies—and consequently multiple temperatures—must be considered. A visual representation of the energy modes commonly used in quantum physics can be seen in Figure 2.1.

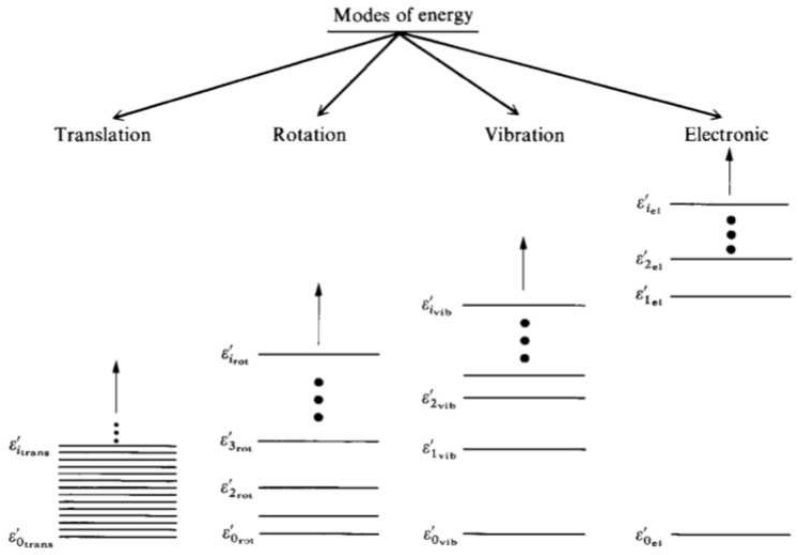

Figure 2.1: Internal degrees of freedom and energy levels. Figure taken from [4].

In gas dynamics it is common to include at least two temperatures in the balance equations, separating the contributions of vibrational-electronic modes at a temperature T_{vib} from the roto-translational ones at temperature T [55, 46]. A similar argument can be made to describe chemical reactions, whose rates determine if a stable mixture composition can be reached shortly after a change in flow conditions. To assess the interaction between flow dynamics, energy levels, and chemistry, it is useful to define their characteristic times τ_{flow}, τ_{vib}, and τ_c, assuming that rototranslational modes immediately adapt to changes in the thermodynamic state. When these three timescales have comparable magnitude, it indicates that energy mode interactions and chemical reactions occur on a timescale comparable to the flow dynamics. Therefore, a state of general thermo-chemical nonequilibrium emerges. In such a state interactions between flow, energy levels, and chemistry are intimately linked and influence each other concurrently.
By comparing τ_{flow} with τ_c and τ_{vib} independently, the situation can be assessed using nondimensional numbers known as Dämkohler numbers. For nonequilibrium chemistry the number is defined as $Da = \tau_{flow}/\tau_c$. Three limiting cases can emerge from its definition:

1. $Da \gg 1$: The flow is near chemical equilibrium, as chemical reactions occur significantly faster than the flow dynamics.

2. $Da \sim 1$: The flow is out of chemical equilibrium, indicating that a new stable composition is reached further downstream.

3. $Da \ll 1$: The flow is *frozen*, meaning that chemical reactions do not have enough time to alter the composition of the mixture, which remains approximately constant.

It is important to note the distinction between frozen and equilibrium states: in frozen conditions, the composition that emerges is not necessarily the stable one for that particular thermodynamic state, but reactions are so slow that changes in composition are unnoticeable. A similar approach applies to thermal nonequilibrium, where the thermal Dämkohler number $Da_v = \tau_{flow}/\tau_{vib}$ compares the flow timescale with the timescale for vibrational energy transfer. In system (2.1), a single energy equation was introduced, as this work will only address chemical nonequilibrium. However, using a two-temperature model would increase the accuracy of the study.

2.2.1 Chemical thermodynamics

The first topic of discussion will be mixtures thermodynamics. In a plasma wind tunnel environment is generally safe to assume that each species behaves as a perfect gas, since deviations from the perfect gas law are minimal at pressures lower than 1000 *bar* and temperatures above 30 K, where intermolecular forces can't be neglected and real gas equations of state become essential [27]. Exceptions to ideal gas behavior can be seen in some species such as CO_2, where molecular interactions become pronounced over a broader range of distances.
A first distinction to be made is between various types of perfect gases, as high temperature gases often do not conform to the assumption of constant specific heats, c_v and c_p.

1. A *thermally perfect* gas is one that satisfies the perfect gas equation of state $p = \rho RT$.

2. A *calorically perfect* gas is a thermally perfect gas for which the specific heat coefficients do not depend on temperature.

Although the second assumption is more common in traditional applications, the first definition is more flexible when dealing with a wide range of temperatures. This hypothesis suggests that all thermodynamic properties of the gas are functions of temperature alone, rather than depending on two or more

variables.
From this point forward, each species will be treated as a thermally perfect gas:

$$p_i = \rho_i R_i T, \tag{2.3}$$

where $R_i = \mathcal{R}/W_i$, with $\mathcal{R}$ indicating the universal gas constant, which is the same for every perfect gas, and and W_i is the molecular weight of species i. The composition of the mixture is often studied in terms of different types of concentration. The mass fraction and mole fractions are defined as:

$$Y_i = \frac{\rho_i}{\rho}, \quad X_i = \frac{p_i}{p}. \tag{2.4}$$

It follows from this definition that $\sum_i X_i = \sum_i Y_i = 1$. For a thermally perfect gas, since the specific heats are a function of temperature alone, internal energy and enthalpy can be expressed respectively as:

$$de_i = c_{v_i}(T)dT, \quad dh_i = c_{p_i}(T)dT. \tag{2.5}$$

Using the perfect gas law, the two specific heat must satisfy:

$$c_{p_i}(T) - c_{v_i}(T) = R_i, \tag{2.6}$$

which indicates that the complexity of the model lies only on the specific form of one of the specific heat coefficient. The rigorous approach to derive the analytical expressions for c_v and c_p consists of finding the energy levels associated with the Hamiltonian function of each internal Degree Of Freedom (DOF) with quantum mechanics and then applying rules of statistical mechanics to compute each contribution to the overall specific heat of the species. These results often need to be corrected by incorporating interactions between the DOFs in order to factor in energy exchanges, thereby complicating the development of an accurate theory. The interest reader can consult [27, 15, 17] for comprehensive derivations. An alternative model is provided by the NASA databases [14], where experimental data are used to fit either a seven-term or a nine-term expression for the species entropy. For instance, the NASA-9 database expresses the molar specific heat at constant pressure for species i, $\hat{c}_{p_i}^{\,o}(T)$, computed at a reference pressure p^o, as:

$$\frac{\hat{c}_{p_i}^{\,o}(T)}{R_i T} = -a_{i,0}T^{-2} - a_{i,1}T^{-1} + a_{i,2} + a_{i,3}T + a_{i,4}T^2 + a_{i,5}T^3 + a_{i,6}T^4, \tag{2.7}$$

where the hat denotes molar specific quantities. Direct integration of $\hat{c}_{p_i}^{\,o}(T)$ and $\hat{c}_{p_i}^{\,o}(T)/T$ provides respectivly the molar enthalpy $\hat{h}_i^o(p,T)$ and the molar entropy $\hat{s}_i^o(T)$ of the species. The coefficients are given by different authors in numerous ranges of temperature, for example in [14]. It is this last model that will be employed in the present work.

Mixtures

Once species thermodynamics has been chosen, it is crucial to specify how the mixture properties are linked to the invidual species. For ideal gases, Dalton law of partial pressures states that the mixture pressure p is completely specified once the individual species pressures are known:

$$p = \sum_{i=1}^{N_s} p_i, \tag{2.8}$$

By defining the mixture gas constant and molar weight as

$$R = \sum_{i=1}^{N_s} R_i Y_i, \quad W = \sum_{i=1}^{N_s} W_i X_i, \tag{2.9}$$

it follows that the mixture behaves like a perfect gas. Mixture specific internal energy u and enthalpy h can be also computed as a linear combination of the single species properties:

$$u = \sum_{i=1}^{N_s} u_i Y_i, \quad h = \sum_{i=1}^{N_s} h_i Y_i, \tag{2.10}$$

while mixture entropy has an additional term due to mixing. Even though for an individual species the specific heats calculation is straight-forward, mixtures need a more careful analysis. By the chain rule

$$c_p = \sum_{i=1}^{N_s} \left[\left(\frac{\partial h_i}{\partial T} \right)_p Y_i + h_i \left(\frac{\partial Y_i}{\partial T} \right)_p \right]. \tag{2.11}$$

The formula clearly indicates that, even if individual species are thermally perfect, the resulting mixture may not exhibit perfect thermodynamic behavior. In the limits of high and low Da, the equation reduces respectively to

$$\begin{aligned} c_{p_{fr}} &= \sum_{i=1}^{N_s} c_{p_i} Y_i, \\ C_{p_{eq}} &= \sum_{i=1}^{N_s} \left[c_{p_i} Y_i + h_i \left(\frac{\partial Y_i}{\partial T} \right)_p \right]. \end{aligned} \tag{2.12}$$

The firs equation shows that a frozen mixture behaves like a thermally perfect gas. However, in a state of thermodynamic equilibrium, the same conclusion does not apply. In this condition, although the composition may vary with temperature and pressure, mixture specific heat it remains dependent solely

on two thermodynamic variables. Lastly, if the mixture is out of equilibrium, defining $\left(\frac{\partial Y_i}{\partial T}\right)_p$ becomes problematic, due to its dependence on the varying mixture composition.
Non-equilibrium conditions provoke a similar issue in the definition of the speed of sound. By definition:

$$c^2 = \left(\frac{\partial p}{\partial \rho}\right)_s. \tag{2.13}$$

In the limiting cases of frozen and equilibrium conditions, from (2.12), two unambiguous results arise:

$$\begin{aligned} c_{fr}^2 &= \frac{c_{p_{fr}}}{c_{v_{fr}}} RT \\ c_{eq}^2 &= \frac{c_{p_{eq}}}{c_{v_{eq}}} \frac{1 - \frac{\rho^2}{p}\left(\frac{\partial u}{\partial T}\right)_T}{1 - \rho\left(\frac{\partial h}{\partial p}\right)_T}. \end{aligned} \tag{2.14}$$

Disturbances with periods much longer than the chemical reaction time τ_c propagate at the equilibrium speed c_{eq}, while those with periods shorter than τ_c propagate at the frozen speed c_{fr}. In nonequilibrium conditions however, disturbances with intermediate periods have a variable propagation speed. Numerical implementations of nonequilibrium flow solvers rely on this choice for the calculations. Comparisons between these two expressions will be shown in section 3.4.

2.2.2 Chemical kinetics

The next topic to address is the source term $\dot{\omega}_i$ in the species mass balance equation (2.1). Changes in partial densities can arise not only from convection but also from chemical reactions with other species. Air at room temperature is a mixture of different gases, mainly molecular nitrogen N_2 at roughly 79%, molecular oxygen O_2 at approximately 21%. Other species such as carbon dioxide CO_2 and neon accout for less than 1%. This equilibrium composition can be altered by varying the thermodynamic variables, namely pressure and temperature. For instance, at 1 atm, O_2 starts to dissociate at around 2000 K, combining with N_2 to initially forms NO, while pure N_2 dissociation begins at 3500 K. Ionization of NO begins at 4000 K while N^+ and O^+ appear at temperatures higher than 6000 K. The lower the pressure, the lower the temperature range at which the dissociation reactions take place. Therefore depending on the temperature and pressure range, we can distinguish among three main mixtures models:

1. Air-5 with N_2, O_2, NO, O, N, when dissociation is present but ionization is negligible.

2. Air-7, when molecular NO^+ ionization appears alongside free electrons e^-.

3. Air-11, when pure species ionization is significant, with the addition of N_2^+, O_2^+, N^+, O^+.

Even if inlet temperatures will often exceed 10000 K, the main interest will be the gas behavior near the probe, where the temperature is lowered by the presence of an isothermal wall. Consequently, a model of Air-5 will be used, characterized by the reactions of thermal dissociation, where molecular species collide with another species X and break apart, and bimolecular exchange, where nitrogen monoxide is formed. These reactions are described in Table 2.2.

Thermal dissociation	**Bimolecular exchange**
$\mathrm{O_2 + X \rightleftharpoons O + O + X}$	$\mathrm{O_2 + N \rightleftharpoons NO + O}$
$\mathrm{N_2 + X \rightleftharpoons N + N + X}$	$\mathrm{N_2 + O \rightleftharpoons NO + N}$
$\mathrm{NO + X \rightleftharpoons N + O + X}$	

Table 2.2: Chemical reactions in an Air-5 mixture, adapted from [10].

To couple the flow with finite rate chemistry in the species mass balance laws (2.1), it is important to recollect the rules of chemical kinetics. To construct the final expression, it is advantageous to begin with a well-known reaction in standard air, such as the thermal dissociation of molecular nitrogen:

$$\mathrm{N_2 + X \underset{k_b}{\overset{k_f}{\rightleftharpoons}} 2\,N + X},$$

where k_f and k_b are forwards and backwards reaction rates. Denoting the molar fractions with brackets, the evolution of $[N_2]$ is governed by the law of mass action:

$$\frac{\mathrm{d}[N_2]}{\mathrm{d}t} = -k_f[N_2][X] + k_b[N]^2[X], \tag{2.15}$$

Generalizating this argument to a number N_r of generic reactions, each involving N_s species X_i, balanced with stoichiometric coefficients $\nu'_{i,r}$ for reactants and $\nu''_{i,r}$ for products, of the form

$$\sum_{\mathrm{i=1}}^{\mathrm{N_s}} \nu'_{\mathrm{i,r}}\ \mathrm{X_i} \underset{k_b}{\overset{k_f}{\rightleftharpoons}} \sum_{\mathrm{i=1}}^{\mathrm{N}} \nu''_{\mathrm{i,r}}\ \mathrm{X_i}, \quad \forall r = 1, .., N_r, \tag{2.16}$$

is immediate. Using (2.4), the extention of the law of mass action for the production rate of ρ_i is [55]:

$$\dot{\omega}_i = W_i \sum_{r=1}^{N_r} (\nu''_{i,r} - \nu'_{i,r}) \left[k_{f,r} \prod_{j=1}^{N_s} \left(\frac{\rho_j}{W_j} \right)^{\nu'_{j,r}} - k_{b,r} \prod_{j=1}^{N_s} \left(\frac{\rho_j}{W_j} \right)^{\nu''_{j,r}} \right]. \tag{2.17}$$

The forward and backward reaction rates $k_{f,r}$ and $k_{b,r}$ can be computed from kinetic theory, but this approach often too complex to implement. Instead, a semi-empirical modified Arrhenius law is typically preferred:

$$k_{f,r} = A_r T^{a_r} e^{-\frac{E_{a,r}}{k_b T}}, \tag{2.18}$$

where $E_{a,r}$ is the activation energy, a_r and $A_r > 0$ are constants. Even though the main interest will be nonequilibrium flows, the composition at the inlet, at a given thermodynamic state, will be computed assuming chemical equilibrium. In this condition the forward and backwards reaction rates for a generic reaction r, $k_{f,r}$ and $k_{b,r}$, are constrained to the equilibrium constant $K_{c,r}$ by the law

$$K_{C,r} = \frac{k_{f,r}}{k_{b,r}}.$$

It can be proven that $K_{C,r}$, when approaching equilibrium conditions, is only a function of temperature that obeys [45, 4]:

$$\log K_{c,r}(T) = -\sum_{i=1}^{N_s} \frac{(\nu''_{i,r} - \nu'_{i,r})\hat{g}_i(T)}{RT} - \log RT \sum_{i=1}^{N_s} (\nu''_{i,r} - \nu'_{i,r}) \tag{2.19}$$

where $\hat{g}_i(T) = \hat{h}_i(T) - T\hat{s}_i(T)$ is the molar Gibbs free energy. It is crucial to emphasize that when a species participates in multiple reactions, there exist corresponding equilibrium constants for each reaction. The computation of these equilibrium constants can leverage statistical mechanics principles, but the outcome strongly depends on the thermodynamic model.

2.2.3 Transport properties

As outlined in previous sections, high temperature flows demand not only a robust thermodynamic model but also a precise description of how mass, momentum, and energy are transported in space under the influence of pressure, velocity, temperature, and possibly other factors such as electromagnetic fields. The couplings between these properties are encapsulated by viscosity, conductivity, and diffusivity. Even though in low-temperature flows these coefficients are often treated as experimental constants, kinetic theory offers a more rigorous and realistic treatment by considering the underlying molecular dynamics

within the fluid. This framework can be used to derive both the expressions for these coefficients based on fundamental physical principles, rather than semi-empirical laws. The former approach will be discussed next.
Traditionally, the bridge between macroscopic properties and microscopic collisional models is givn by the Champman-Enskog approximation of the Boltzmann equation, which governs the evolution of a probability density functions $f_i(\mathbf{r}, \mathbf{u}_i, t)$ in the phase space of species i [51, 26]:

$$\frac{\partial f_i}{\partial t} + \mathbf{u}_i \cdot \nabla_{\mathbf{r}} f_i + \mathbf{F}_i \cdot \nabla_{\mathbf{u}_i} f_i = \sum_{j=1}^{N_s} J_{ij}(f_i, f_j), \tag{2.20}$$

where the subscripts in the gradients indicate the variable used in the differentiation, $\mathbf{F}_i$ are the forces acting on the molecules, $\mathbf{r}$ is the position and $\mathbf{u}_i$ is the species velocity, while the right-hand side describes the collisions occurring in the gas. To infer macroscopic observable quantities from the information provided by f the idea is to integrate over the velocities. For instance the number density is defined as

$$n_i = \int f_i(\mathbf{r}, \mathbf{u}_i, t) d\mathbf{u}_i.$$

The mean value of a generic property of the species $\varphi_i(\mathbf{r}, \mathbf{u}_i, t)$ is given by:

$$\bar{\varphi}_i(\mathbf{r}, t) = \frac{1}{n_i} \int \varphi_i(\mathbf{r}, \mathbf{u}_i, t) f_i(\mathbf{r}, \mathbf{u}_i, t) d\mathbf{u}_i. \tag{2.21}$$

If φ depends on $I = 1, .., N$ internal degree of freedoms the same reasoning is used, with a sum over the internal degrees of freedom to extened the mean value definition. The properties associated with the five choices

$$\varphi_i = m_i, \quad m_i \mathbf{u}_i, \quad \frac{1}{2} m_i \|\mathbf{u}_i\|^2 + \sum_{I=1}^{N} e_i^I, \tag{2.22}$$

where e_i^I is the internal energy of the I-th degree of freedom, are called respectively mass, momentum and total energy density of the i-th species. Mixture density and velocity are defined as:

$$\rho = \sum_{i=1}^{N_s} \rho_i, \quad \mathbf{u} = \frac{1}{\rho} \sum_{i=1}^{N_s} \rho_i \mathbf{u}_i \tag{2.23}$$

The flux associated with a generic quantity φ_i is defined as:

$$\mathbf{\Phi}_i(\mathbf{r}, t) = \int \varphi_i(\mathbf{r}, \mathbf{u}_i, t) \mathbf{U}_i f_i(\mathbf{r}, \mathbf{u}_i, t) d\mathbf{u}_i. \tag{2.24}$$

It is important to emphasize that the property φ_i is transported through the mixture by the peculiar[1] velocity

$$\mathbf{U}_i = \mathbf{u}_i - \mathbf{u}. \tag{2.25}$$

The fluxes associated with the choices

$$\varphi_i = m_i, \quad m_i\mathbf{U}_i, \quad \frac{1}{2}m_i\|\mathbf{U}_i\|^2, \tag{2.26}$$

computed by means of (2.24), are called mass flux $\mathbf{J}_i$, stress tensor $\boldsymbol{\sigma}_i$ and heat flux $\boldsymbol{q}_i$. Moreover, the contribution of peculiar kinetic energy can be identified with the translational component of the internal energy of the species:

$$\frac{3}{2}k_bT_i(\mathbf{r},t) = \frac{1}{n_i}\int \frac{1}{2}m_i\|\mathbf{U}_i\|^2 f_i(\mathbf{r},\mathbf{u}_i,t)d\mathbf{u}_i, \tag{2.27}$$

where k_b is the Boltzmann constant and T_i is the temperature of the species. To find the expressions for these fluxes, the Chapman-Enskog method constists of expanding the probablity density function $f_i = f_i^0(1+\epsilon\phi_i)$ with respect the small parameter ϵ, which can be identified as Kn. In absence of internal degrees of freedom, the solution for f_i^0 is a Maxwellian distribution

$$f_i^0 = n_i\left(\frac{m_i}{2\pi k_bT_i}\right)^{\frac{3}{2}} e^{-\frac{m_i\|\mathbf{U}_i\|^2}{2k_bT}}, \tag{2.28}$$

representing the equilibrium state of the gas. The perturbation term satisfies a linear integro-differential equation, from which a general expression depending on multiple coefficients can be derived [11]:

$$n\boldsymbol{\phi}_i = -\sum_{j=1}^{N_s} D_i^j\mathbf{u}_i\cdot\mathbf{d}_j + A_i\mathbf{U}_i\cdot\nabla\ln T + B_i\left(\mathbf{U}_i\otimes\mathbf{U}_i - \frac{1}{3}\|\mathbf{U}_i\|^2\right) : \nabla\mathbf{u} + \\ + F_i\nabla\cdot\mathbf{u}, \tag{2.29}$$

where

$$\mathbf{d}_j = \nabla X_j + \left(X_j - \frac{\rho_j}{\rho}\right)\nabla\ln p. \tag{2.30}$$

This term is called vector of driving forces. It is vital to stress that mass transport of one species is coupled to other mass fractions by D_i^j, which is a precursor of the diffusivity matrix D_{ij}. This analytical expression enables the

[1] or relative

rigorous computation of the fluxes defined in (2.24). Because the perturbation depends on multiple factors, theoretically, every flux does as well. Despite some contributions being identically zero in heat and mass flux, the main challenge remains solving integral equations for the coefficients themselves. To overcome the lack of closed-form solutions, the coefficients can be approximated using Sonine polynomials. However, the significant computational expense involved in solving the resulting linear systems for the coefficients of the polynomial expansion discourages the analytical approach in favor of empirical laws, even though efforts have been made to improve the efficiency of numerical algorithms. In ordinary fluid mechanics, mass diffusivity D, shear and bulk viscosity μ, λ, and thermal conductivity κ, lead respectively to the well-known Fick, Newton and Fourier laws. Coupled effect such as Soret and Dufour, that account for temperature and mole gradients influence, respectively, on mass and heat transfer, are often neglected. For a deeper discussion about transport phenomena the interested reader can consult [26, 51, 55, 29, 23].
In this thesis, mass flux is truncated considering only mole gradients effects with a fully coupled multi-component Fick law, disregarding baro and thermal diffusion:

$$\mathbf{J}_i = \rho_i \mathbf{U}_i = -\rho \sum_{j=1}^{N_s} D_{ij} \nabla X_j, \tag{2.31}$$

where the diffusion matrix coefficients D_{ij} are computed directly from kinetic theory. In order to lower the computational time, the algorithm used in the solver is:

$$\begin{aligned} \mathbf{J}_i = \rho_i \mathbf{U}_i &= -\rho D_{i,m} \frac{W_i}{W} \nabla Y_i + \rho_i \sum_{k=1}^{N_s} D_{k,m} \frac{W_k}{W} \nabla Y_k, \\ D_{i,m} &= \frac{1 - Y_i}{\sum_{j \neq i} \frac{X_j}{D_{ij}}}, \end{aligned} \tag{2.32}$$

The mixture heat flux incorporates standard heat condution, due to heavy particle collisions, and and particle diffusion, disregarding other contributions. The general form is:

$$\mathbf{q} = -\kappa_F \nabla T + \sum_i \rho_i h_i \mathbf{U}_i. \tag{2.33}$$

Often, the model is formulated in terms of an overall conductivity κ_T, automatically incorporating the previous effects, plus a correction due to roto-vibrational and electronic energy modes κ_E:

$$\kappa_T = \kappa + \kappa_R + \kappa_E, \tag{2.34}$$

where effective heat condution effect due to particle diffusion is

$$\kappa_R = -\sum_{i=1}^{N_s} \rho_i h_i \sum_{j=1}^{N_s} \left(D_{ij} \frac{\partial X_j}{\partial T} \right). \tag{2.35}$$

The inclusion of this contribution will be analyzed in section 3.4, where a comparison between κ and κ_R is shown.

Nondimensional numbers

As already outlined in the previous section, transport properties can be combined into various dimensionless numbers to estimate their relative effects. Since particle diffusion is the only newly introduced mechanism, thermal conductivity and viscosity can be compared with mass diffusivity by defining the Lewis and Schmidt numbers as follows:

$$Le = \frac{\kappa}{\rho D c_p}, \quad Sc = \frac{\mu}{D\rho}. \tag{2.36}$$

It is trivial to check that these numbers are related to the Prandtl number by $Pr \cdot Le = Sc$. Recalling from (2.12) that a single c_p can not be defined, it is worth mentioning thar most softwares use c_p^{Fr} for computational purposes.

2.2.4 Balance laws

The aim of this last subsection on nonequilibrium flows is to briefly summarize the derivation of the system (2.1) and describe how the aforementioned effects are naturally incorporated in ths framework. Without loss of generality, the Boltzmann equation (2.20) can be written in compact form as:

$$\mathcal{D}_i(f_i) = J_i. \tag{2.37}$$

The rate of change of mass, momentum, energy, or any property φ_i, can be obtained by multiplying (2.37) by φ_i and integrating over $\mathbf{u}_i$:

$$\int \varphi_i \mathcal{D}_i(f_i) d\mathbf{u}_i = \sum_{j=1}^{N_s} \int \varphi_i(\mathbf{r}, \mathbf{u}_i, t) J_i d\mathbf{u}_i. \tag{2.38}$$

This forms the basis for the governing equations of any species quantity, once an explicit expression for f_i has been chosen. Mixture balance laws, such as Euler or Navier-Stokes equations, can be derived by summing up individual species equations. In particular, substituting the Maxwellian distribution (2.28) in (2.37) yields the Euler equations, characterized by the absence of

fluxes, while adding the first order perturbation (2.29) results in the Navier-Stokes system. The emerging equations are precisely the ones described in (2.1), which can be written as:

$$\begin{aligned}
\frac{\partial(\rho Y_i)}{\partial t} + \nabla \cdot (\rho Y_i \mathbf{u}) &= -\nabla \cdot \mathbf{J}_i + \dot{\omega}_i, \quad \forall i \in \{1, N_s\} \\
\frac{\partial(\rho \mathbf{u})}{\partial t} + \nabla \cdot (\rho \mathbf{u} \otimes \mathbf{u}) &= -\nabla p + \nabla \cdot \boldsymbol{\tau} \\
\frac{\partial(\rho E)}{\partial t} + \nabla \cdot (\rho H \mathbf{u}) &= -\nabla \cdot \mathbf{q} + \nabla \cdot (\boldsymbol{\tau} \boldsymbol{u}) + \dot{\omega}_T,
\end{aligned} \tag{2.39}$$

with constitutive laws:

$$\begin{aligned}
\boldsymbol{\tau} &= \mu \left[(\nabla \mathbf{u}) + (\nabla \mathbf{u})^T - \frac{2}{3} (\nabla \cdot \mathbf{u}) \mathbb{1} \right] \\
\mathbf{q} &= -\kappa \nabla T + \rho \sum_i h_i Y_i \mathbf{U}_i, \\
\mathbf{J}_i &= \rho_i \mathbf{U}_i = -\rho \sum_{j=1}^{N_s} D_{ij} \nabla X_j, \quad X_j = Y_j \frac{W_j}{W}, \\
h &= h_i Y_i \\
p &= \rho R T.
\end{aligned} \tag{2.40}$$

This form of species mass balance can be derived using (2.4) and (2.25), stressing the role of diffusion velocity as the source of a flux. The term $\dot{\omega}_i$ represents the density change due to chemical reactions and is computed as in (2.17), coupling gas dynamics and chemical kinetics. Mixture mass conservation can be recovered by summing up all the species mass balance laws, noting that chemical reactions must be balanced, thus imposing $\sum_{i=1}^{N_s} \dot{\omega}_i = 0$, and that diffusive fluxes satisfy the constraint $\sum_{i=1}^{N_s} \mathbf{J}_i = 0$. A similar procedure can be applied to the mixture momentum balance. Given that the gas is assumed to be dilute and that electromagnetic interactions do not occur, there is no momentum exchange between the species. Consequently, solving the momentum equation for each species individually is unnecessary. Instead, by summing up all the individual momentum conservation equations, a single mixture momentum balance law can derived. The stress tensor has already been separated as a sum of thermodynamic pressure p and viscous tensor $\boldsymbol{\tau}$, with Stokes' hypothesis considered valid. Since there no external force applied on the mixture, the source term $\rho \mathbf{f} = 0$. Lastly, the single energy balance is a consequence of thermal equilibrium assumption, where the pressure contribution has been separated from viscous stresses with the definition of total enthalpy $H = E + \frac{p}{\rho} = h + \frac{1}{2}\rho \|\mathbf{u}\|^2$. In reactive flows literature, it is common pratice to identify the coupling between chemistry and heat flux by separating sensible

enthalpy from enthalpy of formation:

$$h_i(T) = \underbrace{\int_{T_0}^{T} c_{p_i} dT}_{\text{sensible}} + \underbrace{h^0_{f,i}}_{\text{formation}}, \tag{2.41}$$

where T_0 is a reference temperature, emphasizing the contribution of heat released or absorbed by chemical reactions. With this distinction, the source term that emerges naturally in the energy equation is [4, 47]:

$$\dot{\omega}_T = -\sum_{i=1}^{N_s} \dot{\omega}_i h^0_{f,i}, \tag{2.42}$$

Since this thesis aims at solving these equations numerically it is useful to write the previous equations in the form of a system of conservation laws with a non-zero source term:

$$\frac{\partial \mathbf{U}}{\partial t} + \nabla \cdot \mathbf{F_c} = \nabla \cdot \mathbf{F_d} + \mathbf{S}, \tag{2.43}$$

where $\mathbf{U}$ is the state vector, $\mathbf{F}_c$ and $\mathbf{F}_d$ are convective and diffusive fluxes, and $\mathbf{S}$ is the source term:

$$\mathbf{F}_c = \begin{pmatrix} \rho_i \mathbf{u} \\ \rho \mathbf{u} \otimes \mathbf{u} + p\mathbb{1} \\ \rho \mathbf{u} H \end{pmatrix}, \quad \mathbf{F}_d = \begin{pmatrix} -\mathbf{J}_i \\ \boldsymbol{\tau} \\ \boldsymbol{\tau}\mathbf{u} - \mathbf{q} \end{pmatrix}, \quad \mathbf{S} = \begin{pmatrix} \dot{\omega}_i \\ \mathbf{0} \\ \dot{\omega}_T \end{pmatrix} \tag{2.44}$$

In this study two-dimensional axisymmetric samples will be excusively considered. For one of the formulations in terms of cylindrical coordinates the interested reader can consult [42].
The previous system governs the dynamics of flow at every point around the sample but does not provide a direct insight into heat transfer near the body. However, accurately predicting stagnation point heat flux, where maximum heat transfer occurs, is crucial for successful capsule design. Therefore, the boundary layer region, where viscous effects are dominant, holds particular significance in these studies.

2.3 Reactive boundary layers

For low Reynolds numbers, such as those found in plasma wind tunnels, the large pressure gradients and high heat transfer rates typically maintain the forward boundary layer region in a laminar state. This conditions allows for an analytical treatment of the boundary layer dynamics. This section will follow the approach outlined in Anderson [4].

Assuming a steady state and neglecting radiative heat transfer, two-dimensional reactive boundary layers can be studied with the same assumptions as inert ones. Introducing characteristic variables denoted with the subscript ∞, nondimensional quantities can be written as:

$$\bar{x} = \frac{x}{L}, \qquad \bar{y} = \frac{y}{L}, \tag{2.45}$$

$$\bar{u} = \frac{u}{U_\infty}, \quad \bar{v} = \frac{v}{U_\infty}, \tag{2.46}$$

$$\bar{\rho} = \frac{\rho}{\rho_\infty}, \quad \bar{p} = \frac{p}{\rho_\infty U_\infty^2}. \tag{2.47}$$

$$\bar{\mu} = \frac{\mu}{\mu_\infty}, \quad \bar{e} = \frac{e}{c_v T_\infty}, \tag{2.48}$$

where $\bar{x}$ and $\bar{y}$ are the nondimensional coordinates along and normal to the body, respectively. Mixture continuity and momentum equations become:

$$\begin{aligned}
&\frac{\partial \bar{\rho}\bar{u}}{\partial \bar{x}} + \frac{\partial \bar{\rho}\bar{v}}{\partial \bar{y}} = 0 \\
\bar{\rho}\bar{u}\frac{\partial \bar{u}}{\partial \bar{x}} + \bar{\rho}\bar{v}\frac{\partial \bar{u}}{\partial \bar{y}} &= -\frac{1}{\gamma Ma_\infty^2}\frac{\partial \bar{p}}{\partial \bar{x}} + \frac{1}{Re_\infty}\frac{\partial}{\partial \bar{y}}\left[\bar{\mu}\left(\frac{\partial \bar{v}}{\partial \bar{x}} + \frac{\partial \bar{u}}{\partial \bar{y}}\right)\right] \\
\bar{\rho}\bar{u}\frac{\partial \bar{v}}{\partial \bar{x}} + \bar{\rho}\bar{v}\frac{\partial \bar{v}}{\partial \bar{y}} &= -\frac{1}{\gamma Ma_\infty^2}\frac{\partial \bar{p}}{\partial \bar{y}} + \frac{1}{Re_\infty}\frac{\partial}{\partial \bar{x}}\left[\bar{\mu}\left(\frac{\partial \bar{v}}{\partial \bar{x}} + \frac{\partial \bar{u}}{\partial \bar{y}}\right)\right],
\end{aligned} \tag{2.49}$$

where Re_∞ and Ma_∞ are the Reynolds and Mach number defined by the freestream characteristic quantities. If the examined region is a flat plate of length L, which is assumed to be of unit length without loss of generality, and the boundary layer thickness is of order δ, the magnitudes of the dimensionless variables are of order:

$$\bar{x} \sim O(1), \quad \bar{y} \sim O(\delta) \tag{2.50}$$

with $\delta \ll L$. This immediately implies:

$$\frac{\partial}{\partial \bar{x}} \ll \frac{\partial}{\partial \bar{y}}, \quad \frac{\partial^2}{\partial \bar{x}^2} \ll \frac{\partial^2}{\partial \bar{y}^2}. \tag{2.51}$$

Since in the boundary layer $\bar{u}$ varies from 0 at the wall to 1 at the edge, where freestream conditions are imposed, $\bar{u} \sim O(1)$. Performing an order or magnitude analysis on the mixture continuity equation suggests $\bar{v} \sim O(\delta)$. In the limit of high Reynolds numbers $Re_\infty^{-1} \sim O(\delta^2)$ continuity and momentum

equations (2.49) reduce to:

$$\begin{aligned} \frac{\partial \bar{\rho}\bar{u}}{\partial \bar{x}} + \frac{\partial \bar{\rho}\bar{v}}{\partial \bar{y}} &= 0 \\ \bar{\rho}\bar{u}\frac{\partial \bar{u}}{\partial \bar{x}} + \bar{\rho}\bar{v}\frac{\partial \bar{u}}{\partial \bar{y}} &= -\frac{1}{\gamma M_\infty^2}\frac{\partial \bar{p}}{\partial \bar{x}} + \frac{1}{Re_\infty}\frac{\partial}{\partial \bar{y}}\left(\mu\frac{\partial \bar{u}}{\partial \bar{y}}\right) \\ \frac{\partial \bar{p}}{\partial \bar{y}} &= 0. \end{aligned} \tag{2.52}$$

In term of dimensional variables the system becomes:

$$\begin{aligned} \frac{\partial \rho u}{\partial x} + \frac{\partial \rho v}{\partial y} &= 0 \\ \rho u\frac{\partial u}{\partial x} + \rho v\frac{\partial u}{\partial y} &= -\frac{\partial p}{\partial x} + \frac{\partial}{\partial y}\left(\mu\frac{\partial u}{\partial y}\right) \\ \frac{\partial p}{\partial y} &= 0, \end{aligned} \tag{2.53}$$

which implies $p = p(x)$. The same argument can be directly applied to the reactive system (2.44), which can be wrriten as:

$$\begin{aligned} \rho\left(u\frac{\partial Y_i}{\partial x} + v\frac{\partial Y_i}{\partial y}\right) &= \dot{\omega}_i - \frac{\partial J_{y,i}}{\partial y} \\ \rho\left(u\frac{\partial u}{\partial x} + v\frac{\partial u}{\partial y}\right) &= -\frac{\mathrm{d}p_e}{\mathrm{d}x} + \frac{\partial}{\partial y}\left(\mu\frac{\partial u}{\partial y}\right) \\ \rho\left(u\frac{\partial h}{\partial x} + v\frac{\partial h}{\partial y}\right) &= u\frac{\mathrm{d}p_e}{\mathrm{d}x} + \mu\left(\frac{\partial u}{\partial y}\right)^2 - \frac{\partial q_y}{\partial y}. \end{aligned} \tag{2.54}$$

For this simplified analysis, the gas is considered as binary mixture of heavy and light particles. Consequently, diffusive fluxes are computed using Fick law:

$$J_{y,i} = -D_{i,m}\frac{\partial Y_i}{\partial y}, \quad i = 1, 2. \tag{2.55}$$

This consitutive relation disregards completely not only the role of cross-effects of thermal and baro-diffusion, but also the coupling between the mass fluxes given by the more general diffusivity tensor D_{ij}. However, the most notable consequence follows from the transport property constraint $\sum_i \mathbf{J}_i = 0$. It is easy to check that this implies $D_1 = D_2$. This means that heavy and light particles diffuse into each other's flow with the same efficiency, ignoring the difference in the nature of the species. Inserting this equation into Equation 2.33 produces a boundary layer heat flux of

$$q_y = -\kappa\frac{\partial T}{\partial y} - \rho\sum_i D_{im}h_i\frac{\partial Y_i}{\partial y}. \tag{2.56}$$

This expression, evaluated at $y = 0$, yields the stagnation point heat flux q_w. The boundary condition imposed on the body is a no-slip isothermal wall, coupled with partial recombination:

$$u(x,0) = 0, \quad v(x,0) = 0, \quad T(x,0) = T_w \quad \dot{\omega}_{i,c} = \rho D_{im} \frac{\partial Y_i}{\partial y}. \tag{2.57}$$

The boundary conditions at the edge of the kinematic, thermal, and chemical boundary layers are prescribed as freestream conditions, which are determined through a separate inviscid analysis. To find q_w, Fay and Riddel [25] employed the Howarth-Mangler coordinate transformation proposed by Lees [39] to the system (2.54) governing a binary mixture of molecules. The transformation is defined as follows:

$$\begin{aligned} \xi &= \int \rho_w \mu_w u_e R^{2k} dx, \\ \eta &= \frac{R^k u_e}{\sqrt{2\xi}} \int \rho dy, \end{aligned} \tag{2.58}$$

where the subscripts w and e respectively indicate the evaluation at the wall and at the edge of the boundary layer, and near stagnation point. The parameter k is utilized to automatically include the treatment of two-dimensional ($k = 0$) and for axisymmetric ($k = 1$) bodies with radius of revolution R. The new coordinates ξ and η represent the new streamwise and normal coordinates relative to the wall. The dependent variables within the boundary layer are transformed as follows:

$$\frac{u}{u_e} = \frac{\partial f}{\partial \eta} = f', \quad \frac{h}{h_e} = g(\xi,\eta), \quad \frac{Y_i}{Y_{i,e}} = z_i(\xi,\eta), \tag{2.59}$$

The idea to derive an equivalent system in terms of f, g, z_i is showing that f plays the role of a compressible streamfunction ψ. Transforming the coordinates, the dependent variables, and neglecting the derivatives in the ξ direction, as in classical boundary layer theory, yields the system of partial differential equations:

$$\begin{aligned} (lf'')' + ff'' + \frac{2\xi}{u_e}\frac{du_e}{d\xi}\left(\frac{\rho_e}{\rho} - f'^2\right) &= 0 \\ fg' + \left(\frac{l}{Pr}\right)g' + \frac{u_e^2}{h_e}\left[\left(1 - \frac{1}{Pr}\right)f'f''\right]' + \left(l\frac{Le-1}{Pr}\sum_i \frac{Y_{i,e}}{h_{i,e}}h_i z_i'\right) &= 0 \\ fz_i' + \left(\frac{l}{Sc}z_i'\right)' + 2\xi\dot{\omega}_i\left(\rho_w\mu_w u_e^2 r^{2j}\rho Y_{i,e}\right)^{-1} &= 0, \end{aligned} \tag{2.60}$$

where $l = \rho\mu/\rho_w\mu_w$. The transformed boundary conditions can be found in [4]. The self-similarity of this system is compromised by the reactive and diffusive

terms, which still depend on the ξ coordinate even though derivatives in the streamwise directions have been neglected. However, since the boundary layer thickness is small in hypersonic conditions, the flow is slowed down enough for the incompressibility conditions to be used in the stagnation region. In addition, close to the stagnation point the distance from the wall is so small that the radius of revolution can be approximated with the x-coordinate of the body. A sketch of the stagnation region is shown in Figure 2.2.

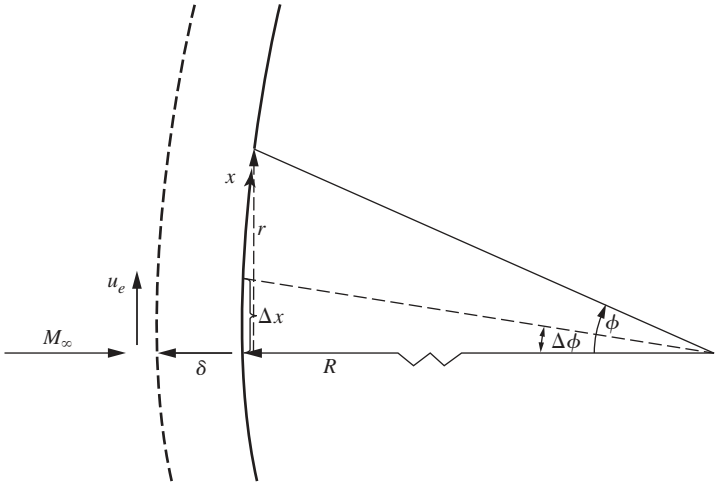

Figure 2.2: Reference frame for stagnation point analysis, from [6].

The conditions respectively translate to:

$$u_e \sim \left(\frac{\mathrm{d}u_e}{\mathrm{d}x}\right)_s x, \quad R(x) \sim x. \tag{2.61}$$

Note that within this reference frame, at the stagnation point, x is orthogonal to the stagnation line. Therefore, u_e represents the vertical component of the incoming velocity at the boundary layer edge. In contrast, numerical solvers typically adopt a fixed reference frame where u is parallel to the stagnation line. Inserting (2.61) in the coordinate transformation (2.58) and substituting the results in the system (2.60), the ξ dependency is finally eliminated, recovering the self-similar behavior of stagnation point reactive flow. From this system of ordinary differential equations, the following expression for stagnation point heat flux q_w with $Le = 1$ was derived by Fay and Riddell [25]:

$$q_{w,1} = 0.76(Pr)^{-0.6} \left(\rho_e \mu_e\right)^{0.4} \left(\rho_w \mu_w\right)^{0.1} \left(\frac{\mathrm{d}u_e}{\mathrm{d}x}\right)_s^{0.5} \left(H_e - h_w\right), \tag{2.62}$$

where the subscript s indicates the evaluation at stagnation point, H_e is the total enthalpy at the edge of the boundary layer and h_D is the dissociation enthalpy of the mixture:

$$h_{D,e} = \sum_{i=1}^{N_s} Y_{i,e} h^0_{f,i}. \tag{2.63}$$

For $Le \neq 1$ the correction is:

$$\frac{q_w}{q_{w,1}} = \left[1 + (Le^{\alpha} - 1)\left(\frac{h_D}{H_e}\right)\right] \tag{2.64}$$

The parameter $\alpha = 0.52$ for an equilibrium boundary layer and $\alpha = 0.63$ for a frozen boundary layer with a fully catalytic wall. Allowing an arbitrary catalycity in a frozen boundary layer, Goulard [31] found

$$q_w = 0.664(Pr)^{-\frac{2}{3}} (\rho_e \mu_e)^{0.5} \left(\frac{\mathrm{d}u_e}{\mathrm{d}x}\right)_s^{0.5} H_e \left[1 + \left(Le^{\frac{2}{3}}\phi - 1\right)\left(h_{D,e}\frac{y_e}{H_e}\right)\right], \tag{2.65}$$

where the factor ϕ encapsulates the catalysis. Supposing the wall boundary conditions are fixed, the stagnation point heat flux is determined by four parameters: density, enthalpy, chemical composition, and the velocity gradient. Assuming local thermodynamic equilibrium in the freestream, the density can be expressed as a function of pressure (p_e) and enthalpy (h_e). As a consequence, these formulas reveal that only three key parameters, $p_e, H_e, \beta_e = (du_e/dx)_s$, are needed to replicate stagnation point heat flux in hypersonic flight conditions. This insight is particularly valuable, as it suggests that subsonic tests can accurately predict the maximum heat flux, providing a significant advantage in probe design. The interested reader can consult the original paper by Kolesnikov [37] to read more about this approach called Local Heat Trasnfer Simulation (LHTS).

2.4 Extrapolation to flight

Following the similarity, peak heat flux duplication can be achieved by imposing the three matching conditions:

$$H_{e,f} = H_{e,g}, \quad p_{e,f} = p_{e,g}, \quad \beta_{e,f} = \beta_{e,g}, \tag{2.66}$$

where subscripts f and g are used respectively for flight and ground quantities. Since the boundary layer edge is considered the limit for an inviscid analysis,

the first two conditions can be directly imposed using momentum and energy conservation along the stagnation line [8]:

$$\begin{aligned} p_{\infty,f} + \rho_{\infty,f} V_{\infty,f}^2 &= h_{\infty,g} \\ h_{\infty,f} + \frac{1}{2} V_{\infty,f}^2 &= p_{\infty,g}, \end{aligned} \tag{2.67}$$

where the subscript ∞ is used to indicate freestream conditions. The assumption of hypersonic flow allows the further simplification

$$p_{\infty,f} \ll \rho_{\infty,f} V_{\infty,f}^2, \quad h_{\infty,f} \ll V_{\infty,f}^2. \tag{2.68}$$

In the third equation, the velocity gradients can be analytically derived for spherical bodies. The velocity is expressed in both cases using Bernoulli equation:

$$u = \sqrt{\frac{2(p_e - p)}{\rho_e}}, \tag{2.69}$$

where p and u are pressure and velocity along the body. The coordinate along the body x can be approximated near stagnation point as in Figure 2.2:

$$x \sim R\phi, \tag{2.70}$$

where ϕ is the small deflection angle and R is the radius of the body. The pressure distribution over a hemispherical capsule in hypersonic flow is given by Newtonian theory [4]:

$$p_f = p_{e,f} \cos^2 \phi + p_{\infty,f} \sin^2 \phi, \tag{2.71}$$

Substituting in (2.69) and differentiating with respect to x yields:

$$\beta_{e,f} = \frac{1}{R} \sqrt{2 \frac{(p_{e,f} - p_{\infty,f})}{\rho_{e,f}}} \tag{2.72}$$

The same reasoning is applied for the subsonic velocity gradient. The pressure distribution over a spherical body of radius R is given by subsonic potential flow [38]:

$$p_g = p_{e,g} - \frac{9}{4} \sin^2 \phi (p_{e,g} - p_{\infty,g}). \tag{2.73}$$

which results in [13]:

$$\beta_{e,g} = \frac{3}{2} \frac{1}{R_c} \sqrt{\frac{2p_{e,g}}{\rho_{e,g}} \left(1 - \frac{p_{\infty,g}}{p_{e,g}}\right)} = \frac{3}{2} \frac{U_{\infty,g}}{R_c}. \tag{2.74}$$

For non spherical bodies the radius R is subtituted by an effective radius R_{eff}, defined as the equivalent sphere radius that would yield the same velocity gradient. While the thermodynamic properties in subsonic flow can be measured either directly or indirectly, the evaluation of the velocity gradient at the edge of the boundary layer is a more delicate matter. A classical way to find the velocity gradient β_e at stagnation point from a viscous simulation is to extrapolate the inviscid solution to the wall, interpreting the boundary layer edge as the inflection point of the velocity gradient along the stagnation line. A sketch of the method is in Figure 2.3.

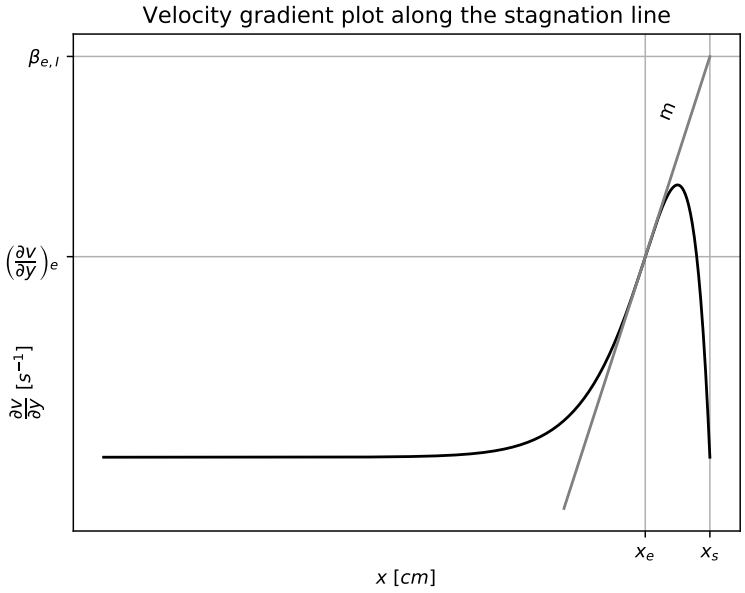

Figure 2.3: Inviscid extrapolation strategy from velocity gradient plot.

The inviscid solution is reconstructed by locating the inflection point and then operating a linear regression in that region. From Figure 2.3 it follows that:

$$\beta_{e,I} = \left(\frac{\partial u}{\partial x}\right)_e + m(x_s - x_e), \tag{2.75}$$

where x_e is the inflection point, x_s is the stagnation point and m is the slope of the tangent to the graph at the inflection point. The subscript i is used to specify the inviscid strategy employed in this procedure.
The main reason to depart from this approach for subsonic high temperature flow is that classical boundary layer theory presumes a high Reynolds number limit. In plasma wind tunnels this is not the case, since the viscosity is generally high and the flow velocity is low. Subsequently, in the stagnation

region, the velocity parallel to the body, u_e, is not significantly greater than the perpendicular component v_e. Moreover, classical boundary layer theory is only strictly valid for flat plates.

2.4.1 Finite thickness boundary layers

A more modern approach involves revisiting the boundary layer equations to incorporate higher-order effects such as the curvature of the body. Higher-order boundary layers were originally studied by Van Dyke [24], and Davis extended these results to encompass the entire viscous shock layer region [22, 21].
Both approaches employ a coordinate transformation, performed with an intrinsic body-fitted reference frame, as in Figure 2.4.

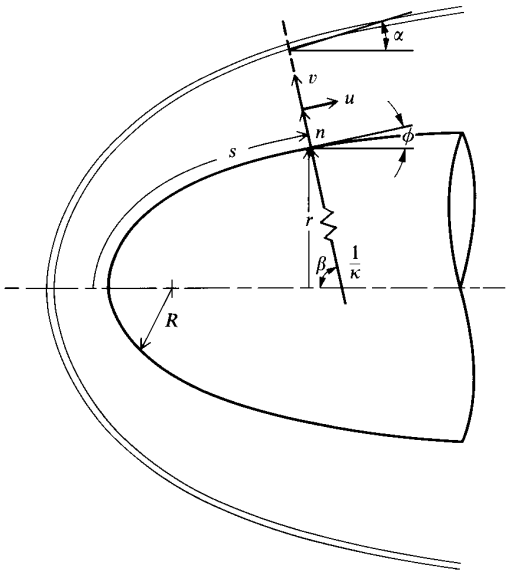

Figure 2.4: Boundary layer and viscous shock layer reference frame, from [4].

The boundary layer region is defined by the ruled surface

$$\mathbf{X}(s, n) = \mathbf{r}(s) + n\mathbf{N}(s), \tag{2.76}$$

where $\mathbf{r}$ is the position along the body, s its the arclegth parameter, and $\mathbf{N}(s)$ its normal vector. The three-dimensional layer is obtained by rotating this surface around the stagnation line. Using Frenet-Serret formulas, the associated three-dimensional metric becomes

$$dl^2 = H^2 ds^2 + dn^2 + R^{2j} d\phi^2, \tag{2.77}$$

where $H = 1 + n\kappa(s)$, κ being the curvature of the body, and $R = (r + n\cos\phi)$ as the local radius of revolution. In this frame a perturbative analysis with the small parameter $\epsilon = \dfrac{1}{\sqrt{Re}}$ is applied to the transformed systems, with the only difference being that the viscous shock layer theory keeps terms of order $O(\epsilon^2)$ in the derivation. The axisymmetry affects only the continuity equation, which becomes in both cases:

$$\frac{\partial}{\partial s}\big(\rho u R^j\big) + \frac{\partial}{\partial n}\big(\rho v H R^j\big) = 0. \tag{2.78}$$

The second order boundary layer momentum equations are:

$$\begin{aligned}\rho\left[\frac{u}{H}\frac{\partial u}{\partial s} + v\frac{\partial u}{\partial n} + \kappa uv\right] &= -\frac{1}{H}\frac{\partial p}{\partial s} + \frac{1}{R}\frac{\partial}{\partial n}\left(\mu R\frac{\partial u}{\partial n}\right) + \kappa\left(\mu\frac{\partial u}{\partial n} - u\frac{\partial \mu}{\partial n}\right)\\ \frac{\partial p}{\partial n} &= \kappa\rho u^2,\end{aligned} \tag{2.79}$$

while the viscous shock layer momentum equations are:

$$\begin{aligned}\rho\left[\frac{u}{H}\frac{\partial u}{\partial s} + v\frac{\partial u}{\partial n} + \kappa uv\right] =& -\frac{1}{H}\frac{\partial p}{\partial s} + \frac{1}{R}\frac{\partial}{\partial n}\left(\mu R\frac{\partial u}{\partial n}\right) + \kappa\left(\mu\frac{\partial u}{\partial n} - \kappa\frac{u}{H}\right) +\\ &+ \frac{\epsilon^2}{HR^j}\frac{\partial}{\partial n}\big(H^2 R^j \tau\big)\\ \frac{\partial p}{\partial n} =& \frac{\kappa}{H}\rho u^2 - \frac{\rho u}{H}\frac{\partial v}{\partial s} - \rho v\frac{\partial v}{\partial n},\end{aligned} \tag{2.80}$$

where

$$\tau = \mu\left(\frac{\partial u}{\partial n} - \frac{\kappa}{H}u\right) \tag{2.81}$$

For a planar flow at stagnation point $k = 0$, $\kappa = 0$, $\phi = \pi/2$. Using $s = x$ and $n = y$, the x-momentum equation simplifies, in both cases, to

$$\rho u\frac{\partial u}{\partial x} + \rho v\frac{\partial u}{\partial y} = -\frac{\partial p}{\partial x} + \frac{\partial}{\partial y}\left(\mu\frac{\partial u}{\partial y}\right), \tag{2.82}$$

while in the y-direction the second order boundary layer becomes

$$\frac{\partial p}{\partial y} = 0, \tag{2.83}$$

and the viscous shock layer reads

$$\frac{\partial p}{\partial y} = -\rho u\frac{\partial v}{\partial x} - \rho v\frac{\partial v}{\partial y}. \tag{2.84}$$

The most notable difference between the two theories is the non-zero pressure gradient in the normal direction, but if the perpendicular velocity is assumed to be small both lead to first order boundary layer system. In classical boundary layer theory, pressure gradients are computed by extrapolating the inviscid solution to the wall, where it is assumed that $v_e = 0$, due to the infinitesimally small thickness of the boundary layer. However, in low Reynolds number flows, it is more appropriate to match the solution to the real boundary layer edge, which is now at a non-negligible distance e from the wall where $v_e \neq 0$. The x-momentum equation, neglecting higher order terms, reads:

$$\left(\frac{\partial p}{\partial x}\right)_e = -\rho_e u_e \frac{\partial u_e}{\partial x} - \rho_e v_e \frac{\partial u_e}{\partial y}, \tag{2.85}$$

where the extra term is a direct consequence of the new matching choice. At stagnation point we can assume the usual incompressible result given by (2.61). Substituting this result in a classical boundary layer for the hypersonic case, and then in a finite thickness boundary layer for the low-Reynolds flow, neglecting high order terms, gives:

$$\begin{aligned} -\frac{1}{x}\left(\frac{\partial p}{\partial x}\right)_{e,f} &= \left(\frac{\mathrm{d}u_e}{\mathrm{d}x}\right)^2 \\ -\frac{1}{x}\left(\frac{\partial p}{\partial x}\right)_{e,s} &= \left(\frac{\partial u_e}{\partial x}\right)^2 + v_e \frac{\partial}{\partial y}\left(\frac{\partial u_e}{\partial x}\right). \end{aligned} \tag{2.86}$$

By comparison it follows that

$$\beta^2_{e,FT} = \left(\frac{\partial u_e}{\partial x}\right)^2 + v_e \frac{\partial}{\partial y}\left(\frac{\partial u_e}{\partial x}\right), \tag{2.87}$$

where the subscript FT indicates finite thickness extrapolation. This last equation will be used alongside (2.75) for numerical extrapolation purposes.

Chapter 3

Numerical methods

This chapter introduces Discontinuous Galerkin methods, outlining their features and the advantages they offer in high temperature gas dynamics. Subsequently, Direct Numerical Simulations (DNS) will be examined, focusing on their challenges and applicability. A concise overview of the solver employed in this thesis will follow. The Mutation++ library will then be introduced as a practical tool for integrating high temperature effects into the solver using efficient algorithms. The library will be utilized for a preliminary analysis of the thermodynamic and transport properties of the flow.

3.1 Discontinuous Galerkin Method

Discontinuous Galerkin (DG) methods are a family of discretization procedures initially developed by Reed and Hill [49] for the numerical solution of neutron transport equations, combining the advantages of both the Finite Element Method (FEM) and the Finite Volume Method (FVM).
The system (2.43) at steady state consists of eight coupled nonlinear reaction-convection-diffusion partial differential equations, with fluxes defined by (2.44). To solve this system numerically, a discretization procedure has to be employed. DG schemes belong to the class of Finite Element Methods, where the domain Ω is partitioned into a finite number of non-overlapping regions Ω_e such that:

$$\Omega = \bigcup_e \Omega_e. \tag{3.1}$$

On each element the solution is decomposed on a basis of a finite dimensional space V_E:

$$u_m \approx \sum_e \sum_{i=0}^{N} U_{i,m}^e \phi_i^e, \tag{3.2}$$

where $U^e_{i,m}$ are the coefficients of this decomposition and $\{\phi^e_i\}$, $i \in \{0, \ldots, N\}$ is a basis of V_E, with the superscript e indicating that the support of the basis function is restricted to the element Ω_e. A Galerkin method consists of choosing the space $V_e \subset V$, where V is the natural space where the weak form of the governing partial differential equation is defined. A Discontinuous Galerkin method is a non-conforming method where $V_e \not\subset V$, in particular the basis functions are regular piecewise polynomials within a single element Ω_e but not necessarily continuous across the boundaries of the elements, thus relaxing the requirement for global continuity of the solution. A sketch of this concept is shown in Figure 3.1.

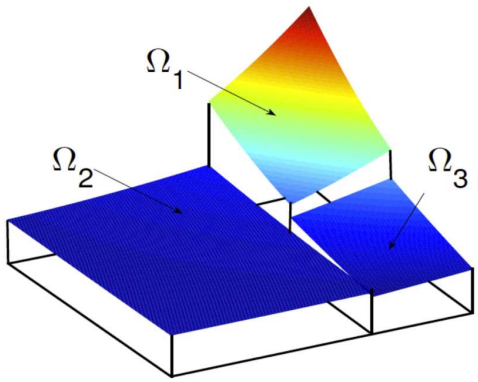

Figure 3.1: A Discontinuous Galerkin approximation of a function, from the Stanford FX Lab website.

Several options are available for the basis selection, but one of the most renowned choices is the Lagrange polynomials. Lagrange polynomials are particularly advantageous due to their simplicity and their ability to interpolate functions accurately within each element. It is crucial to observe that, since no continuity is required on the boundaries, the interface nodes are duplicated, increasing the number of degrees of freedom (DOF) involved in the computations.

Discretization

As in classical finite element methods, it is vital to derive an appropriate variational formulation of a generic reaction-convection diffusion equation for $\mathbf{u}$. Without loss of generality, the m-th equation of the system can be written as:

$$L_m(\mathbf{u}) = -\frac{\partial u_m}{\partial t} + \frac{\partial}{\partial x^k} F^k_{c,m}(\mathbf{u}) - \frac{\partial}{\partial x^k} F^k_{d,m}(\mathbf{u}, \nabla \mathbf{u}) - S(\mathbf{u}, \nabla \mathbf{u}), \tag{3.3}$$

The dependence of the diffusive term on the state vector and its gradient is assumed to be expressed in a Fourier-type law:

$$F^k_{d,m}(\mathbf{u}, \nabla\mathbf{u}) = D^{k,l}_{m,n}(\mathbf{u})\frac{\partial u_n}{\partial x^l}, \tag{3.4}$$

where $D^{k,l}_{m,n}$ is a suitable fourth order tensor that mathematically represent the jacobian with respect to the gradient and physically plays the role of a conductivity or diffusivity tensor.
Multiplying by a test function v, integrating over the partitioned domain $\Omega = \bigcup \Omega_e$, and using generalized divergence theorems for discontinuous functions, yields

$$\begin{aligned}
\int_\Omega v L_m(\mathbf{u}) d\Omega = & \underbrace{\sum_{\Omega_e\in\Omega}\int_{\Omega_e} v\frac{\partial u_m}{\partial t}d\Omega_e}_{T_v} \\
& \underbrace{-\sum_{\Omega_e\in\Omega}\int_{\Omega_e}\frac{\partial v}{\partial x^k}F^k_{c,m}(\mathbf{u})d\Omega_e}_{C_v} + \underbrace{\sum_{I_i\in I}\int_{I_i}[v]^k n^k \mathcal{H}_m\left(\mathbf{u}^+, \mathbf{u}^-, \mathbf{n}\right) dS}_{C_i} \\
& \underbrace{+\sum_{\Omega_e\in\Omega}\int_{\Omega_e}\frac{\partial v}{\partial x^k}F^k_{d,m}(\mathbf{u})d\Omega_e}_{D_v} \underbrace{-\sum_{I_i\in I}\int_{I_i}\left\langle D^{kl}_{mn}\frac{\partial u_n}{\partial x^l}\right\rangle [v]^k dS}_{D_i} \\
& \underbrace{-\theta\sum_{I_i\in I}\int_{I_i}\left\langle D^{k,l}_{m,n}\frac{\partial v}{\partial x^l}\right\rangle [u_m]^k dS}_{D_t} \underbrace{+\alpha\sum_{I_i\in I}\int_{I_i}[v]^k [u_m]^k dS}_{D_p} \\
& \underbrace{-\sum_{\Omega_e\in\Omega}\int_{\Omega_e} vS(\mathbf{u}, \nabla\mathbf{u})d\Omega_e}_{S_v} \qquad \forall v \in V,
\end{aligned} \tag{3.5}$$

where T_v is the unsteady part, C_v and C_i discretize the convective part, D_v, D_i, D_t, D_p arise from Interior Penalty (IP) methods for diffusive fluxes, S_v is the source term, I_i are the interfaces of the element Ω_e, and the jump and average trace operator are defined respectively as

$$\begin{aligned}
[a] &= a^- n^- + a^+ n^+ \\
\langle a\rangle &= \frac{1}{2}\left(a^+ + a^-\right),
\end{aligned} \tag{3.6}$$

with the superscripts indicating internal and external states on the interface.

Convection

The term C_v and C_i in the convective part can be regarded as the high order extention of the classical FVM. The variational form of the one-dimensional scalar convective part of (2.44) is obtained multiplying by a test function v and integrating by parts, which results in

$$\underbrace{\sum_{\Omega_e} \int_{\Omega_e} v \frac{\partial u}{\partial t} d\Omega}_{T_v} - \underbrace{\sum_{\Omega_e} \int_{\Omega_e} \frac{\partial v}{\partial x} F_c(u) d\Omega}_{C_v} + \underbrace{\sum_{I_i} \int_{I_i} v F_c(u) n dS}_{C_i} = 0 \tag{3.7}$$

The boundary term, for convective equations, is treated with a numerical flux similar to the finite volumes approximation, of the form [32]:

$$C_i = \sum_{I_i} \int_{I_i} [v] \mathcal{H}(u^+, u^-, \mathbf{n}) dS. \tag{3.8}$$

To ensure stability, entropy inequality, local extrema diminishing and positivity of the associated Godunov scheme, the flux has to satisfy the notion of E-flux provided by Osher [44]:

$$(\mathcal{H}(u^+, u^-, \mathbf{n}) - F_c(u)) \cdot (u^+ - u^-) \leq 0, \tag{3.9}$$

For higher order schemes the treatment for discontinuities is more complex and can be found in [35].
It is easy to check that, by choosing piecewise constant functions, the term C_v vanishes, and the formulation becomes identical to a first-order semi-discrete FVM, which computes the time evolution of the cell average based upon the flux balance at the boundary of the cell:

$$\frac{\mathrm{d}u}{\mathrm{d}t} - \frac{1}{V_{\Omega_e}} \sum_{I_i} \mathcal{H}(u^+, u^-, \mathbf{n}). \tag{3.10}$$

Riemann problem

Discontinuous Galerkin methods naturally include Riemann problems at each cell interface like classical FVMs. Several options are available. Plasma wind tunnel often deal with compressible flows with very high temperatures, which lead to high speeds of sound (see section 3.4), and consequently low Mach numbers. Compressible solvers in this regime face some numerical convergence challenges due to the disparity between convective and acoustic time scales. The solver needs to resolve both the slow-moving convective phenomena and the fast-moving acoustic waves. This leads to a large number of iterations for convergence because the time step is often limited by the fast acoustic

waves, despite the slow movement of the actual fluid. Preconditioning the time derivatives in the equations helps to scale the different terms appropriately. This makes the solver handle the disparity between acoustic and convective time scales better, leading to more balanced and stable computations. In addition, at low Mach numbers, the flow is dominated by pressure terms. As a result small errors or perturbations in the pressure field can result in large errors in the velocity. The AUSM+up scheme introduced by Liou [40] addresses this by separating pressure and convective terms. This approach helps to correctly capture the pressure field without causing large errors in the velocity field.

Diffusion

Consider a scalar diffusive problem (2.44) with a scalar diffusivity $D(u)$ for simplicity purposes. Multiplying by a test function and integrating yields

$$0 = \sum_{\Omega_e \in \Omega} \int_{\Omega_e} \frac{\partial v}{\partial x} \left(D(u) \frac{\partial u}{\partial x} \right) d\Omega_e - \sum_{I_i \in I} \int_{I_i} v D(u) \frac{\partial u}{\partial x} n dS. \tag{3.11}$$

Once again the interface term is treated with a numerical flux. There several options to discretize this term [7], but this numerical study will employ they Interior Penalty (IP) method for high order polynomials and a Bassi-Rebay second order (BR2) scheme for P_0 approximations. In the first scheme the boundary term is replaced by three new terms:

$$0 = \underbrace{\sum_{\Omega_e \in \Omega} \int_{\Omega_e} \frac{\partial v}{\partial x} \left(D(u) \frac{\partial u}{\partial x} \right) d\Omega_e}_{D_v} \underbrace{- \sum_{I_i \in I} \int_{I_i} \left\langle D(u) \frac{\partial u}{\partial x} \right\rangle [v] dS}_{D_i} \tag{3.12}$$

$$\underbrace{- \theta \sum_{I_i \in I} \int_{I_i} \langle D(u) \frac{\partial v}{\partial x} \rangle [u] dS}_{D_t} + \underbrace{\alpha \sum_{I_i \in I} \int_{I_i} [v][u] dS}_{D_p}, \tag{3.13}$$

While D_i is a term that treats the interace fluxes, in D_t defines the symmetry properties of the resulting bilinear form. Here, $\theta = 1$, $\theta = -1$ and $\theta = 0$ respectively ensure a symmetric (SIP), non-symmetric (NIP) or incomplete (IIP) form. Lastly, D_p is a term that penalizes jumps with parameter α. In principle θ can be chosen chosen freely without affecting consistency, while α can negatively impact the conditioning of the matrix associated with diffusive flux. For more informations on α, one can consult [32] and their references, which are essential for the conditioning of the matrix that emerges from the diffusive flux.
The main reasons to employ IP methods are their stability and simplicity, since

penalties discourage sharp gradients and only direct neighbours of the element are used to evaluate the residuals, lowering the requierd memory and computational time. However, this approach is not consistent when piecewise constant polynomials are employed, since D_b and D_s are identically zero. For this reason, P_0 simulations will rely on the second order Bassi-Rebay (BR2) scheme [12] where reconstructions of the gradients can be derived from discontinuities using *lifting operators*.

Boundary conditions

The discretization scheme at the limit of the domain is treated by implementing boundary conditions. Typically, for the convective part, the ghost cell values are specified and the Riemann problem is solved on the physical boundary of the domain as in classical FVMs. For the diffusive flux Dirichlet, Neumann and Robin boundary conditions have to be implemented. If the Dirichlet boundary condition is an oscillating function, directly imposing it on the boundary nodes can lead to large errors. Nitsche-type schemes use a variational formulation to minimize the average interpolation error between the imposed value and the function, penalizing their difference with a parameter α:

$$\begin{aligned} a(u,v) = \int_\Omega \frac{\partial v}{\partial x}\left(\mu\frac{\partial u}{\partial x}\right)d\Omega + \alpha\int_{\partial\Omega} v(u-u_0)dS - \\ \int_{\partial\Omega} v\left(\mu\frac{\partial u}{\partial x}n\right)dS - \theta\int_{\partial\Omega}(u-u_0)\left(\mu\frac{\partial v}{\partial x}n\right)dS \end{aligned} \tag{3.14}$$

The cost of this operation is the addition of the third term which restores consistency [32]. Finally, the fourth term is a symmetric term.

Linear system assembling

Once the state vector is decomposed into a linear combination of Lagrange polynomials, and the test function is chosen to be a basis function itself, the integrals are computed on a reference element with a change of variables, as shown in Figure 3.2.

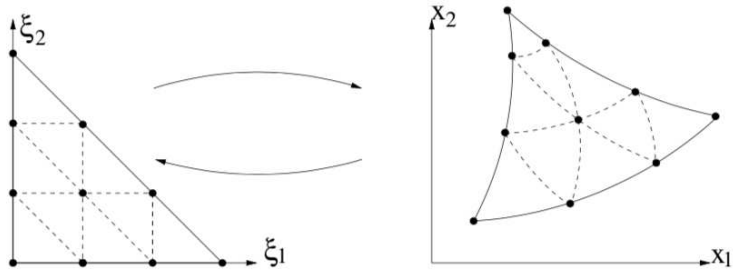

Figure 3.2: Reference element mapping for a generic finite element, from [32].

For interior integrals, it is common to use Gauss-Legendre quadrature, which only involve interior points, while appropriate numerical fluxes are used at the boundaries. Once the integrals and the fluxes are computed, the resulting linear system is to be solved with a suitable numerical method.

Features

The are several advantages of using the Discontinuous Galerkin (DG) method for high temperature flow simulations on unstructured meshes. First When using a basis of polynomials of order p on unstructured meshes, the method guarantees an order of convergence of $p + 1$. In addition they are highly scalable, making them suitable for parallel computing environments and large-scale simulations [18]. They also support *hp* adaptivity , which allows for local mesh refinement (h-refinement) and increasing the polynomial order (p-refinement) in regions where higher resolution is required, improving computational efficiency and accuracy [20]. Moreover they ensure local conservation properties, which is fundamental for accurately simulating reactive flows where conservation of species fractions is critical [41]. They exhibit minimal degradation in accuracy and stability near areas with sudden changes in mesh size or near walls, making them robust for complex geometries and boundary conditions and their dispersion-dissipation properties are favorable [41], as seen in Figure 3.3, which is crucial for non equilibrium flows. The high dissipation at high polynomial orders can be beneficial for underresolved scales. In contrast, other than implementation issues, they consume more memory than standard FVMs, since they need to store polynomial coefficients, flux terms and other information on inter-element coupling. Moreover, low dissipation makes the method sensitive to underresolved features. A study by Gassner et. al. [28] on dissipation-dispersion properties of a DG method used to simulate a one-dimensional scalar advection problem with a pure upwind flux is visible in Figure 3.3. The polynomials degree increas from $N = 1$ up to $N = 10$. The dispersion relation is written as a complex number $\Omega(k)$, where the imaginary

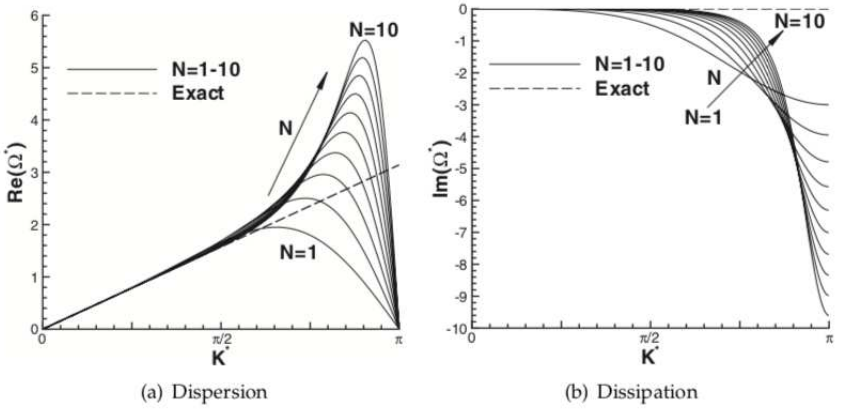

Figure 3.3: Numerical dissipation-dispersion properties of a 1-D DG method, from [28].

part represents dissipation and k is the wavenumber.

3.2 Direct Numerical Simulations

The study performed in this thesis will be conducted with a number of Direct Numerical Simulations (DNS), taking advantage of the scalability properties of a DG method. With this approach the reactive high temperature Navier-Stokes equations are solved without any turbulence modeling. The software resolves all scales of motion, from the largest flow structures down to the smallest dissipative scales by directly integrating the equations of motion. DNS is particularly valuable for studying reactive flows, as the introduction of empirical models could heavily influence the results.
The energy spectrum qualitatively pictured in Figure 3.4 describes how the kinetic energy of turbulence is distributed across different scales or wavenumbers k. In the inertial subrange, energy cascades from larger scales (low k) to smaller scales (high k) without loss due to viscosity, while the dissipative range is dominated by viscous dissipation, which transforms energy into heat. As a result, to capture the full spectrum of turbulent scales a numerical simulation must use a very fine mesh. The required resolution increases with the Reynolds number. From this analysis it can be shown that most of the computational resources are used to simulate the dissipative range, making DNS almost always too expensive to employ for industrial applications.

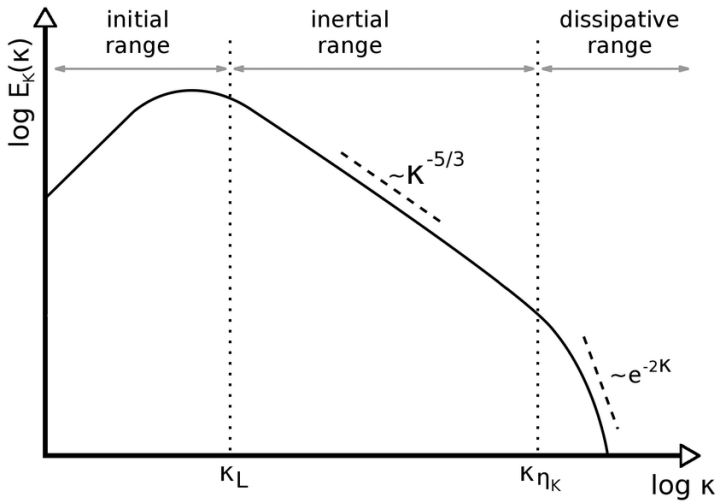

Figure 3.4: Energy spectrum as a function of the wavenumber.

While DNS is generally computationally onerous, for a simple two-dimensional flow over a capsule, the tradeoff between benefits and cost is highly favorable for several reasons:

- Reactive flows are particularly susceptible to changes in temperature and velocity. In this framework, using a turbulence model could disrupt the flow structure, altering the chemical composition of the mixture. DNS avoids this by resolving all scales of motion directly, ensuring an accurate capture of chemical interactions.
- Discontinuous Galerkin Methods are inherently scalable, making them suitable for high fidelity simulations. This scalability allows for efficient parallelization.
- In plasma wind tunnels, the flow typically has low Reynolds numbers. This allows the flow to remain laminar most of the time, reducing the likelihood of turbulence development.

In addition, the aim of this thesis is to support future wind tunnel tests, possibily becoming a reference to run future Large Eddy Simulations (LES). As a consequence it is vital to employ a high fidelity method.

3.3 ARGO software

`ARGO` is a high fidelity and high accuracy CFD software developed at Cenaero which implements a DG scheme to of solve a variety of problems in different

regimes, from incompressible flow to hypersonics. It was originally developed to treat industrial turbomachinery problems with its main module `DGFluid`, which implements different turbulence models. Three more modules have been added through the years, `DGAcoustic`, `DGAM`, primarily for additive manufacturing, thermal and mechanical problems, and `DGAblation`, developed for ablative porous materials and multi-species high enthalpy flow, mainly used for aerospace applications. The solver uses an hybrid parallelization relying on the Message Passing Interface (MPI) and Open Multi-Processing (OpenMP) to deal with costly simulations. The software is coupled with mechanical and thermal solvers for specific problems, as well as with external libraries for post-processing. A beneficial features this study will exploit for nonequilibrium flows computations is the coupling with the external library Mutation++, which will be described in th next section, to accurately model the thermodynamic, kinetic, and transport properties of the mixture.

Simulation strategy

The present work will consist of running a number of steady DNS simulations of the reactive Navier-Stokes system (2.43) on a two-dimensional plane. The simulations are run with the `DGAblation` module, utilizing a variable number of threads depending on the complexity of the mesh on a single core. This choice is due primarily to the robustness of a direct matrix inversion method (Gauss) compared to an iterative solver such as GMRES, which often require careful tuning for convergence and performance in parallel environments. Moreover, a fully parallel computation would imply using user-defined meshes exclusively, as mesh adaptation after partitioning is not feasible. This could lower the overall computational time by reducing mesh complexity and concentrating resources on critical regions.
Each simulation of system is divided into a number of intermediate steps, with the final solution from the previous step injected as the initial condition for the next.

1. A first simulation is run with a P_0 approximation on a user-generated mesh. In this phase the gas is composed of 5 nonreacting species. Thermodynamic and transport properties are still computed with Mutation++, but chemical kinetics is neglected. At the end ad adaptation blocks reduces the complexity of the unstructured portion of the mesh.

2. The second step is almost identical to the first. The only difference is the addition of chemical reactions, using the complete system of equations in (2.43). As of this step velocity gradients cannot be computed, since derivatives of 0-order polynomials are necessarily null. A second

adaptation block further reduces the number of unstructured cells of the mesh.

3. A third simulation is run with a P_2 approximation. A P_2 approximation is in principle sufficient to use (2.87), since second derivatives would belong to P_0. On the other hand, this choice would reduce the overall accuracy to a FV method once again.

4. The final step consists of a P_3 approximation for the state vector $\mathbf{U}$. The results saved by the solver are and automatically organized for post-processing.

The sequence can vary for complex cases, with an occasional addition of split steps and more conservative CFL strategies in order to improve stability and convergence of the solution.

3.4 Mutation++

As outlined in chapter 1, it is vital not only to accurately represent the mixture by considering more reliable models than calorically perfect gases with by ordinary heat conduction, but also to properly include the coefficients dependence, namely specific heats, conductivity, diffusivity and viscosity, on the thermodynamic state. In order to account for those effects, a user-friendly library called Mutation^{++} has been implemented at the von Kárman Institute for Fluid Dynamics [53]. This library offers high accuracy models for high temperature gas mixtures. The properties are computed dirctly from kinetic theory with relatively low cost algorithms. The coupling with CFD softwares is used primarily to update, step by step, the thermodynamic, transport and chemical properties of the flow, providing a realistic description of the species at all times.
The thermodynamic model chosen in a NASA-9 database, more accurate than NASA-7 for temperatures higher than 5000 K, for an Air-5 mixture, neglecting ionization effects. A preliminary calculation of equilibrium composition with different enthalpies can be seen in Figure 3.5.
It is clear that oxygen dissociated at a lower and narrower range of temperatures compared to nitrogen. This model presumes the absence of carbon dioxide, which can drastically change the composition. Furthemore, for this range of temperature an Air-11 model would be more approapriate, since electronic energy modes are excited and ionization cannot, in principle, be neglected. These equilibrium computations will be used to determine the inlet composition from a given thermodynamic state and to compare the effects of different flow conditions on the chemical boundary layer. More details will be given in subsection 4.1.2.

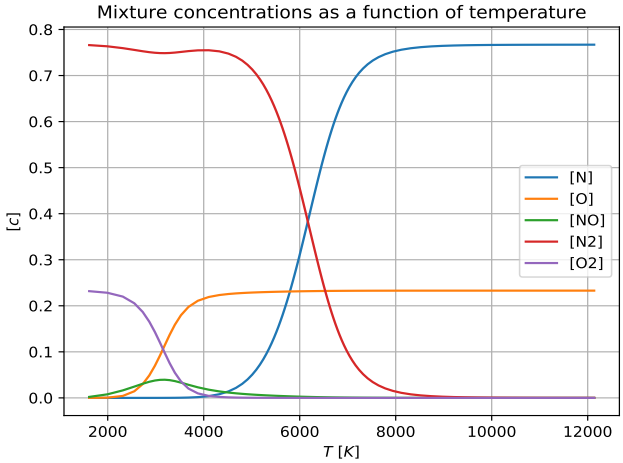

Figure 3.5: Equilibrium composition computed with Mutation++ for an Air-5 model with $p = 100\ mbar$.

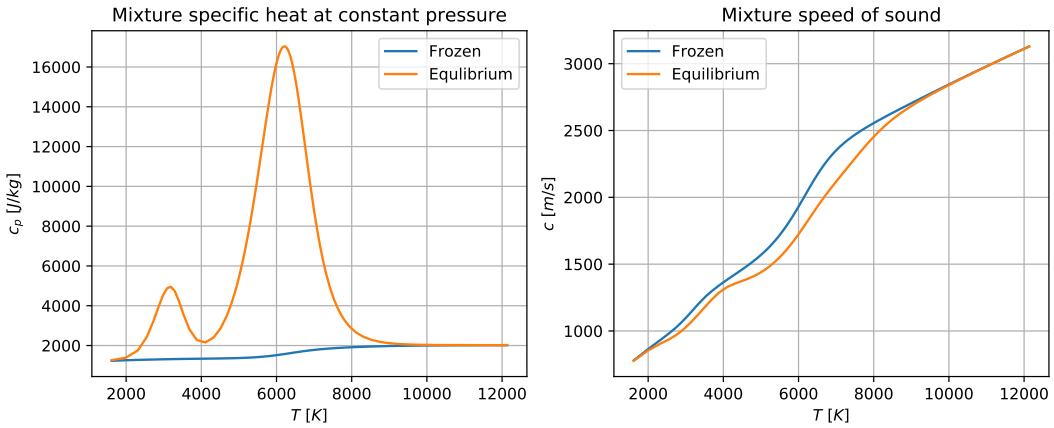

Figure 3.6: Thermodynamics properties computed with Mutation++ for an Air-5 model with $p = 100\ mbar$.

The equilibrium mixture specific heat exhibits a relative maximum when nitrogen monoxide fraction reaches its maximum, while the peak is attained when there an equal concentration of molecular nitrogen N_2 and atomic nitrogen N. The frozen and equilibrium speeds of sound diverge notably when molecular nitrogen begins to dissociate, but converge towards similar values at higher temperatures. For the same range of temperatures transport properties are computed and shown in Figure 3.7.

While viscosity typically increases with temperature for most gases, the second graph underscores the importance of incorporating particle diffusion in high temperature gas dynamics heat transfer modeling (2.33). Effective conductiv-

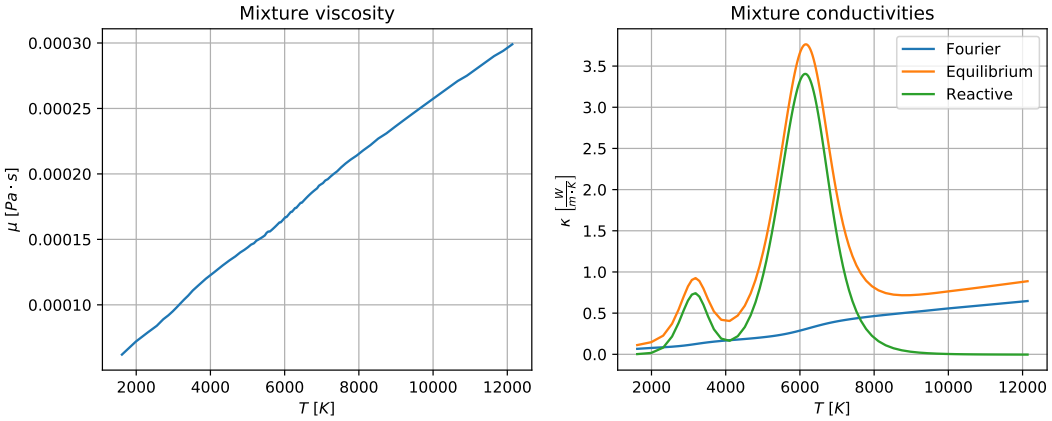

Figure 3.7: Viscosity and conductivity computed with Mutation++ for an Air-5 model with $p = 100\ mbar$.

ity κ_R dominates the overall contribution until high temperatures (8000 K) are reached and chemical reactions cease to be the primary driver, with electronic modes gaining relevance once species are fully dissociated. In an Air-5 model Fourier conductivity emerges as the main factor, as it monotonically increases with temperature. The library will also compute mutlicomponent diffusion coefficients directly from kinetic theory for an accurate description of mass transfer, as described in (2.32).

Chapter 4

Simulations and results

This chapter is dedicated to the description of the pre-processing phase, including geometries, boundary conditions, mesh generation and the algorithms used in the simulation sequence. The post-processing results with varying geometries and boundary conditions will then be presented with special attention to the β parameter. To conclude the thesis, a hypersonic simulation will be used for comparison with a suitable number of subsonic simulations.

4.1 Simulation setup

In this section, a detailed description of the pre-processing steps for the CFD simulations will be provided, with special attention will be given to the challenges associated with automated mesh generation and the numerical parameter extrapolation for various cases with different boundary conditions.

4.1.1 Plasmatron envelope description

The Plasmatron facility located at the von Kárman Institute for Fluid Dynamics is composed of several systems which are described in [16] in great detail. Engineers can adjust generator power to control inlet enthalpy, varying temperature and thus density. They can also manipulate inlet mass flow to adjust the flow velocity of the high temperature air, and pressure, which affects both chemical composition and flow speed. The experimental ranges are summarized in Table 4.1

Within these ranges the sample can be designed with different shapes.Typically, these samples are cylinders with various corner radii, including both hemispherical and sharp-cornered noses.

Physical entity	Range	Unit
h_∞	$[10, 20, 30, 40, 50]$	MJ/kg
p_o	$[40, 55, 70, 85, 100]$	$mbar$
$\dot{m}_\infty$	$[8, 10, 12, 14, 16]$	g/s

Table 4.1: Experimental ranges of the facility used for the simulation.

4.1.2 Computational domain

The computational domain used for simulations is two-dimensional, taking advantage of the axisymmetry of the probe. The outlet is assumed to coincide with the end of the probe for simplicity, as the primary focus is on stagnation point aerothermodynamics and the region behind the sample is not of particular interest. Additionally, the backwards facing step could influence the stability of the simulation. A sketch of the domain is shown in Figure 4.1, with dimensions given in millimeters. The origin of the axes is the inlet, located at $x_o = 10\ cm$, while the stagnation point is fixed at $x_s = 48.5\ cm$. This choice will be justified shortly.

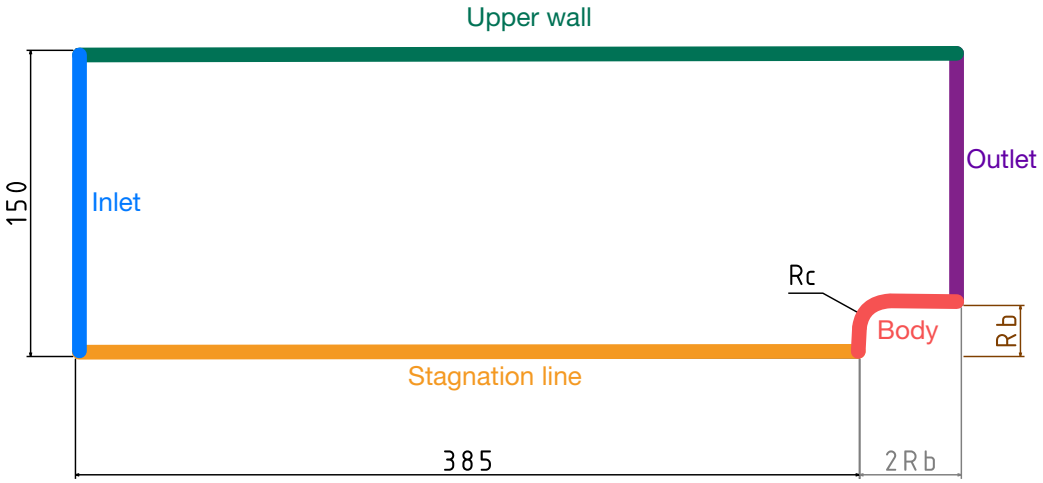

Figure 4.1: Plasmatron test chamber geometry.

Two types of simulations will be considered. A first study has been conducted using a realistic Plasmatron torch profile at the inlet. The boundary conditions applied to this case are summarized in Table 4.2.

Boundary	Condition	Expression
Stagnation line	Symmetry	$\mathbf{u} \cdot \mathbf{n} = \mathbf{0}, \quad \nabla T \cdot \mathbf{n} = \nabla Y_i \cdot \mathbf{n} = 0.$
Body	No-slip isothermal	$\mathbf{u} = \mathbf{0}, \quad T = 350\ K.$
Oulet	Constant pressure	$p = 100\ mbar.$
Upper wall	No-slip adiabatic	$\mathbf{u} = \mathbf{0}, \quad -\mathbf{q} \cdot \mathbf{n} = 0.$
Inlet	Dirichlet	$\mathbf{U} = \mathbf{U}_{cp}(y).$

Table 4.2: Boundary conditions with torch profiles at the inlet.

Since the body is axisymmetric, imposing a symmetric boundary condition on the stagnation line is sufficient to recreate the effects on a halved domain. The body is subjected to an ideal cooling system which maintains a constant surface temperature with no material degradation. Finally, the adiabatic condition on the upper wall imitates the closed and controlled environment of the test chamber. At the inlet a Plasmatron torch profile provided by the engineers at the von Kárman Institute is imposed. The corresponding temperature and velocity profiles are graphed in Figure 4.2 while freestream pressure is fixed at 100 $mbar$.

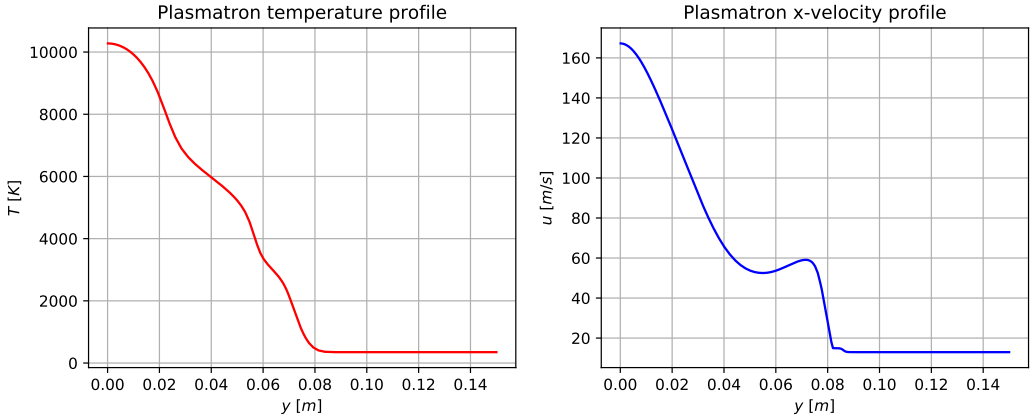

Figure 4.2: Plasmatron torch inlet profiles with a power of 110 kW and $p = 100\ mbar$.

The profile results from the torch geometry shown in Figure 1.4, which heats up only a small portion of the test chamber inlet height. To avoid numerical convrgence issues, a MagnetoHydroDynamic (MHD) code is used to simulate the injection of the plasma flow generated by the torch into a rectangular chamber of variable length L. The outlet profile of this simulation with $L = 10\ cm$ can be provided by VKI's engineers and serves as the inlet for this study. Therefore, to conduct a comprehensive study with realistic Plasmatron profiles a meticulous preliminary work has to be done: the ICP profiles have to

be selected based on the distance with the torch and other physical quantities and at the time this study was conducted a full database of profiles was not available. Moreover, region where velocity and temperature profiles have steep gradients in most cases impact the stability of the simulation, preventing the simulation from reaching the target tolerance and reducing the residuals to the desired level. refinement of this region will add computational cost to the sequence and will be detailed in the next section. A further motivation to avoid torch profiles at the inlet is that the duplication procedure described in section 2.4 is based on the equivalence of freestream quantities and does not account for variable boundary conditions. Finally, it is important to stress that, since this is a first comprehensive study, it relies on simplified models to serve as a general reference. For these reasons the full envelope will be constructed with a constant inlet, but further studies could improve the accuracy of the model by including variable profiles in LHTS theory. For this case new boundary conditions have been chosen. A summary is in Table 4.3.

Boundary	**Condition**	**Expression**
Stagnation line	Symmetry	$\mathbf{u} \cdot \mathbf{n} = \mathbf{0}, \quad \nabla T \cdot \mathbf{n} = \nabla Y_i \cdot \mathbf{n} = 0.$
Body	No-slip isothermal	$\mathbf{u} = \mathbf{0}, \quad T = 350\ K.$
Oulet	Constant pressure	$p = p_\infty.$
Upper wall	Freestream	$\mathbf{u} = \mathbf{u}_\infty, \quad T = T_\infty, \quad Y_i = Y_{i,\infty}.$
Inlet	Dirichlet	$\mathbf{u} = \mathbf{u}_\infty, \quad T = T_\infty, \quad Y_i = Y_{i,\infty}.$

Table 4.3: Boundary conditions with constant inlet.

The most notable difference with Table 4.2 is the freestream boundary condition. The nature of this choice is two-fold:

1. A freestream boundary condition replicates a more open environment, where disturbances cannot reflect on the test chamber, emulating a real flight scenario.

2. While the profile goes to zero when approaching the upper-left corner, constant velocity, temperature and fractions would produce a sharp discontinuity, disturbing the solver stability.

As already outlined, the conditions that von Kárman Institute for Fluid Dynamics' test engineers can control are inlet specific enthalpy, mass flow, and pressure. For this reason the focus will be on these three effects. However, inlet boundary conditions are specified in terms of state vectors such as velocity, temperature, and species fractions, rather than enthalpy and mass flow. Mutation++ has been particularly useful for this purpose because its

`PYTHON` library allows for the creation of interactive scripts. Using the NASA-9 database, the perfect gas equation, and the definition of mass flow, a simple script has been implemented to automatically compute the corresponding thermodynamic variables based on the experimental ranges indicated in Table 4.1. This script also inserts these variables into the ARGO input files. The process consists of implementing a Newton-Raphson method to compute the roots of the function $h(T) - h_\infty$, with h_∞ as the inlet enthalpy, in order to determine the inlet temperature. Once the temperature is known, the density and composition of the mixture at the inlet can be calculated with Mutation++ knowing the inlet pressure, which is imposed directly, and assuming equilibrium. From these values, the velocity is finally determined based on the imposed mass flow. The experimental range used in this thesis is in Table 4.1, even though the facility can employ even higher mass flows and lower pressures.
The two cases described in this sections will require different meshes, as the second case is aimed at improving stability and reducing computational time by ignoring torch profiles. However, this comes at the cost of reduced accuracy in reproducing the actual conditions to which the probes are subjected, including the limited space available inside the test chamber.

4.1.3 Mesh generation

Mesh generation is a crucial component in a CFD simulation. In the context of high temperature gas dynamics, such as flow around capsules and probes, the boundary layer region must be accurately represented to capture chemical recombinations, as well as the kinematic and thermal boundary layers. The latter is especially important for heat transfer calculations. While DG methods excel at providing high accuracy representations with high order polynomials and are less sensitive to mesh generation, mesh quality still plays a role in resolving small scales and improving the simulatio robustness.
To generate the meshes, the software `gmsh` has been used. Its `PYTHON` API allows for parametric mesh generation, which is a practical way of handling multiple geometries with slight variations. This script also accounts for boundary layer refinement and mesh size matching in different regions. The process is optimized allowing curved elements on the body profile.
Two types of meshes have been generated: the first one has been used to study the effect or a real Plasmatron torch profile at the inlet. The profile generates non-isentropic vortex structures that compromise the residuals and thus the stability of the simulation. To stabilize the simulation, it is necessary to refine this region, starting from the upper bound of the plasma torch. The body radius R_b is fixed at 25 mm, while the free parameter is $R_c \in [0, 25]$ mm. One of the meshes is visible in Figure 4.3 with a particular on the boundary layer.

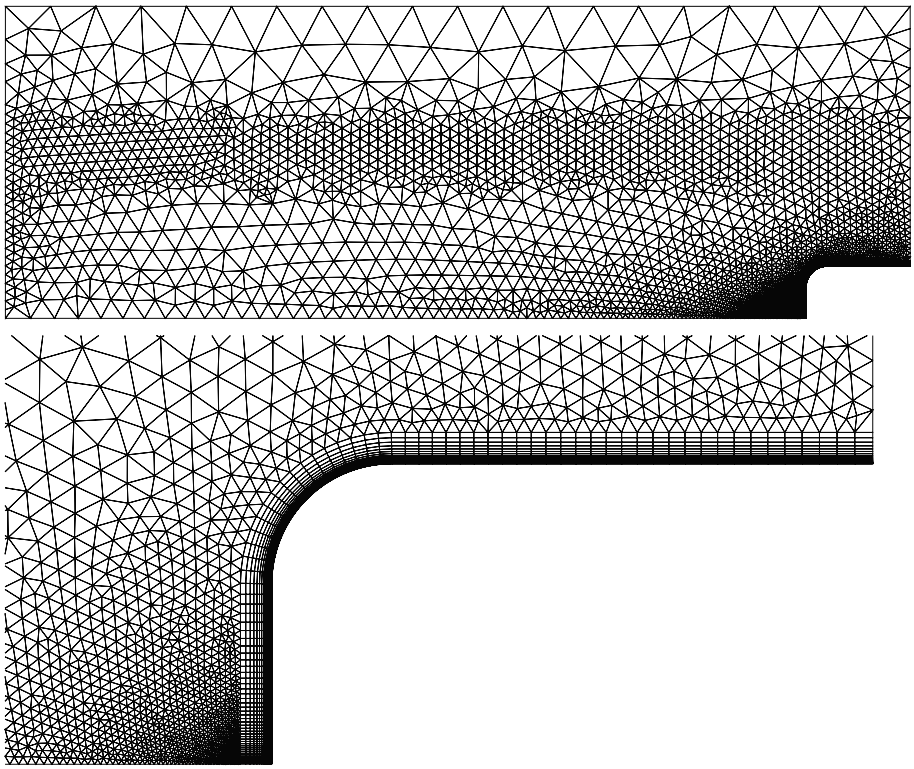

Figure 4.3: Mesh generated to simulate the flow with a torch profile at the inlet.

The refinement will be avoided with a constant inlet to reduce the simulation time.

Automation

The automation of the mesh generation must consider various scenarios, particularly variations in the corner radius exposed to the flow. This value can significantly alter the flow structure, underscoring the importance of boundary layer meshing strategy. This necessitates that the refinement along the probe perimeter varies according to both the length of its sides and the progression factor chosen for cell size reduction. The progressive refinement is vital in three specific regions:

1. A higher resolution along the stagnation line is essential to capture velocity gradients and flow deviation near the probe.

2. The same principle applies to the probe perimeter directly exposed to the flow, with a progression towards the stagnation point.

3. Decreasing R_c results in steeper forward-facing steps and recirculation zones. To ensure robust simulation, it is essential to resolve these scales. Therefore, further refinement is needed as the mesh approaches the corner.

The approach followed in this thesis consists of computing the initial and final cell size of a reference side, such as the stagnation line, based on the length and user-defined geometric progression factors. Fixing the progression on the adjacent side will allow the computation of the number of cells needed for the refinement. The same approach is used for the corner, with the addition of fan points to accommodate rectangular geometries. Since torch profiles vary over very short lengths, a further refinement is needed at the inlet. An example of automated mesh gnerated with the same script as Figure 4.3 is visible in Figure 4.4.

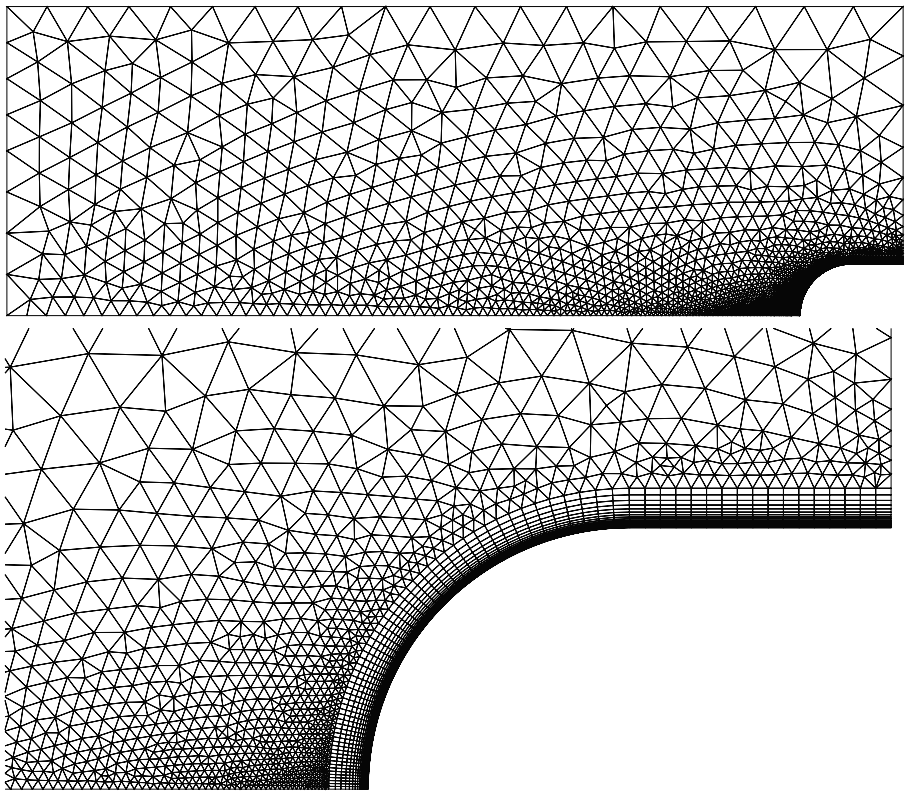

Figure 4.4: Mesh generated automatically to study hemispherical probes.

Adaptation

The simulation sequence described in section 3.3 involves two adaptation steps, which are performed automatically by the solver on the triangular elements,

while keeping the quadrangular structured boundary layer mesh intact. The reduction in complexity will be determined by the specific simulation, ranging from 0.75 to 0.85. In Figure 4.5 and Figure 4.6 two adapted meshes are visible.

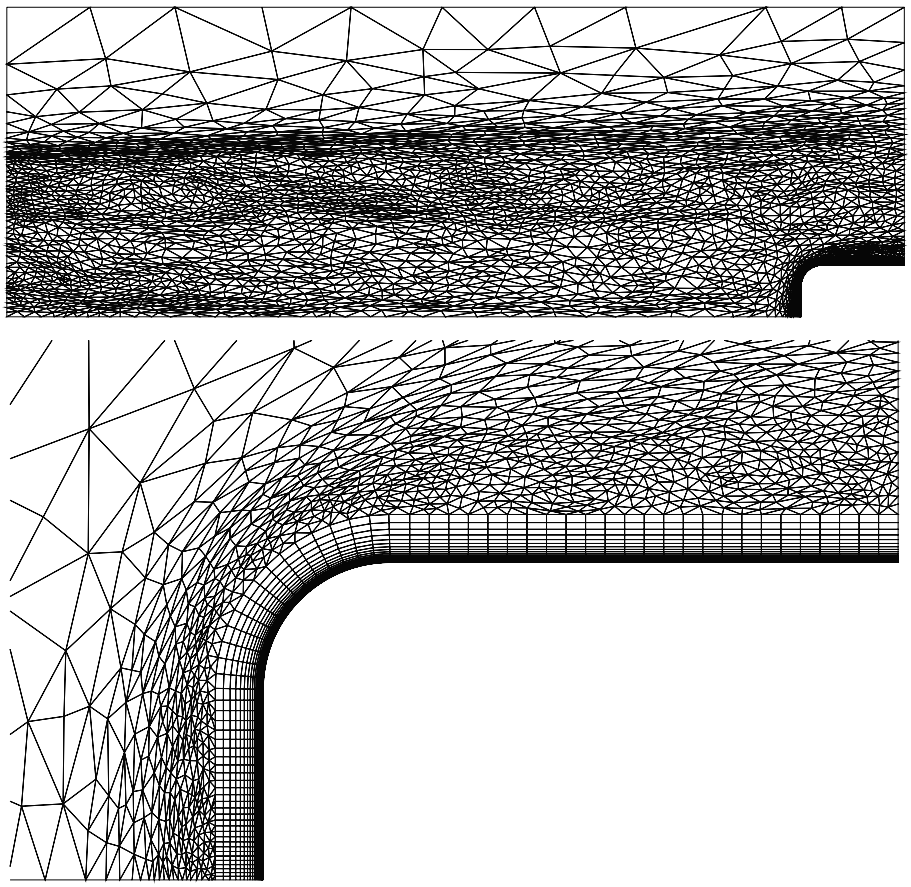

Figure 4.5: Solver adaptation of mesh 4.3.

The adaptation block concentrates the resources on the jet where vorticity is induced by entropy gradients, justifying this refinement strategy.

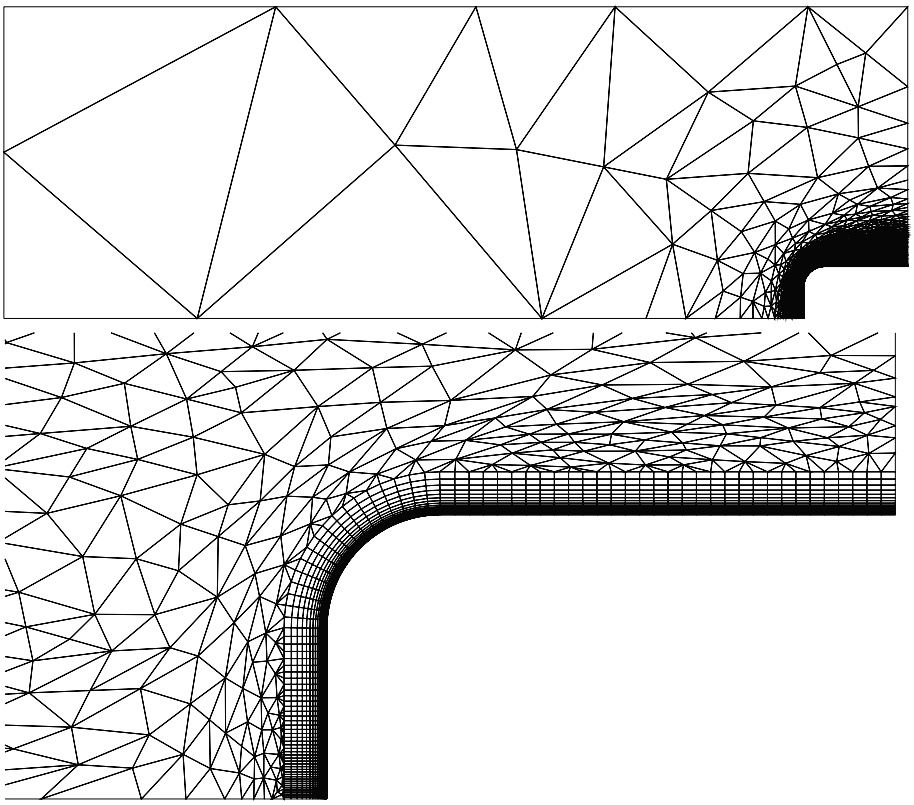

Figure 4.6: Solver adaptation of a mesh generated automatically for a constant inlet case with probe corner radius $R_c = 10\ mm$.

The automatic cell size matching, transitioning from a circular arc to a flat wall, ensures an appropriate distribution of cells. Moreover, it is evident that in this case fewer cells are needed at the inlet, while the number increases in the boundary layer. In the flat plate region the adaptation algorithms is consistent with the flat plate law for boundary layer thickness:

$$\delta(x) \sim \sqrt{x}. \tag{4.1}$$

4.2 Evaluation of the velocity gradient

The numerical analysis of the results is one of the most challenging parts of this thesis. In the evalutation of β using (2.87) the following problems emerge:

1. Even though a P_3 approximation is ideal for all calculations up to the third derivative, a DG method duplicates the DOF on cell boundaries, disrupting injectivity of the solution. To address this issue, a filtering strategy is used on all the data to recover a one-to-one correspondence between stagnation line coordinates and computed quantities.

2. A second issue is that locating the boundary layer edge as the inflection point requires an a-posteriori computation of derivatives of v, which could reduce the order of the approximation if the algorithm is not at least second order. Preliminary work reveals that the inflection is ascending, allowing the search for the maximum of the first derivative instead of the zero of the second derivative, thereby avoiding further accuracy losses.

3. A physical issue in small corner cases is the presence of forward-facing steps, which could seriously alter and compromise the algorithms used to compute β. Recirculation zones negatively impact the solver stability, compromising the sequence and causing the simulation to terminate with a fatal error. Even when this can be avoided with particularly conservative CFL strategies, stiffness is still visible in some cases. Consequently, jumps at the interfaces can become extremely high, and the search algorithm would fail in most of these cases. To overcome this third issue, a two-parameter nonlinear regression is performed solely for the purpose of finding the inflection point.

From this point, both (2.75) and (2.87) will be used to determine the β paramaters. The two methods will be compared to highlight their differences and understand the most sensible approach for this estimation.

4.3 Plasmatron test case

This section is dedicated to the analysis of the facility with the torch inlet presented in Figure 4.2 and the boundary conditions in Table 4.2. As a result, the only parameter analyzed in this preliminary case will be the corner radius R_c in the range $[2, 25]$ mm.

Solver performance

For the case $R_c = 25$ mm, CPU times are in Table 4.4 while residuals are shown in Figure 4.7. The stop criteria are a residual decrease of 10^{-11} for the P_0 cases and 10^{-7} for the P_2 and P_3 cases.
The solver exhibits instability during the initial computation because initial conditions do not satisfy the boundary conditions, which impose different contstraints on the state vector. The initial residual jumps are most significant when adding reactive terms and transitioning from piecewise constant functions to a P_2 approximation. In both cases the step also involves an additional mesh adaptation and a subsequent mesh interpolation during the first iteration, contributing to the residuals increase.

Approximation	Gas	Itation time [s]	Mesh elements
P_0	Frozen	0.64	6705
P_0	Reactive	0.55	6221
P_2	Reactive	6.25	5714
P_3	Reactive	26.79	5714

Table 4.4: Solver performance for a hemispherical probe simulation sequence.

Results

The results of dissociated species mole fractions and temperature profiles near the stagnation point are in Figure 4.8.

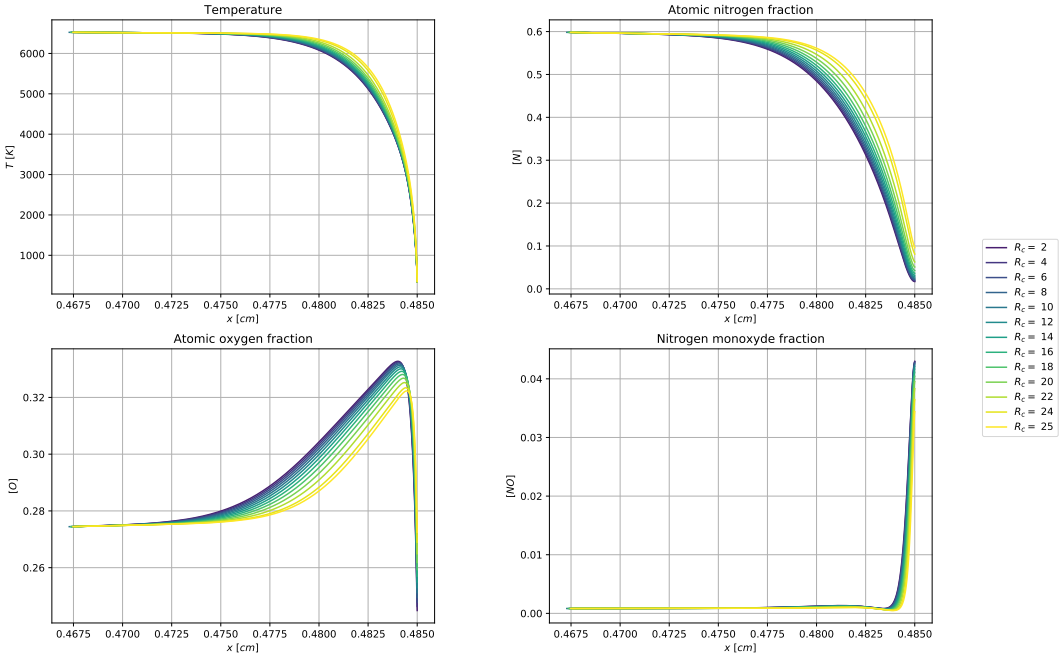

Figure 4.8: Dissociated species mole fractions and temperature along the stagnation line with different corner radii and a torch inlet profile.

The profiles in Figure 4.2 rapidly descend towards very low temperatures, leaving most of the jet and the upper part of the domain in a uniform low-temperature environment. This also causes velocity and temperature to drop before the boundary layer is reached, justifying the usage of an Air-5 model, neglecting ionization effects for stagnation point calculations.
It is evident in every case that chemical equilibrium is not attained in the stagnation point region, as the species fractions do not stabilize at a consistent value. Nitrogen recombination is observed to occur around 6000 K, while

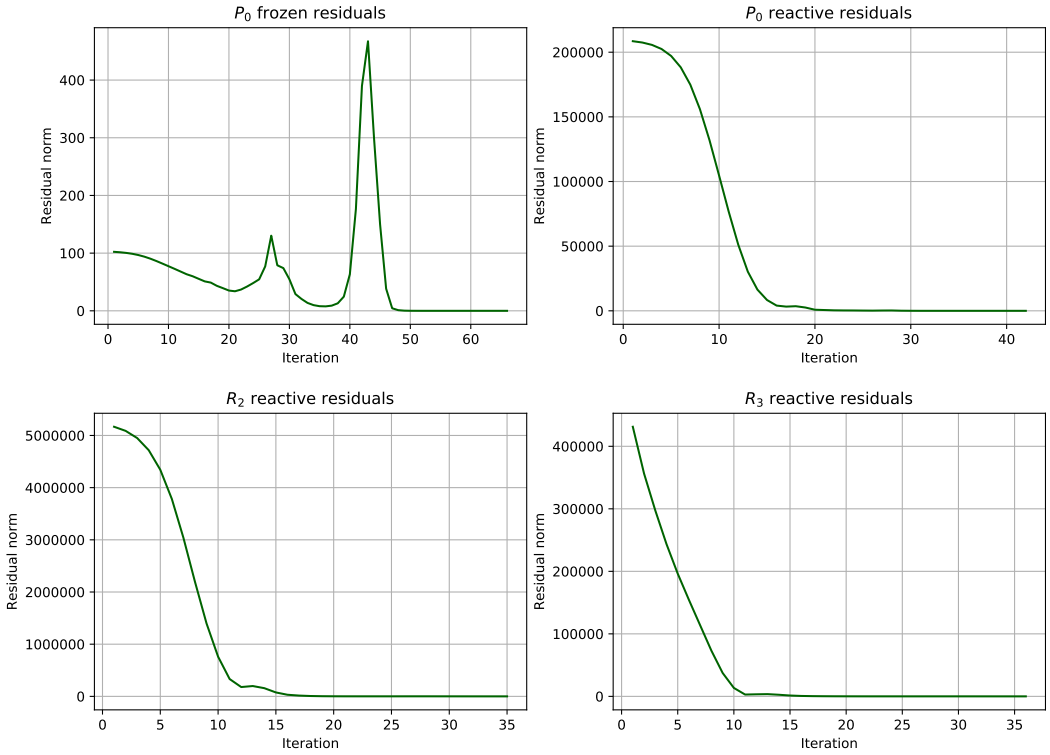

Figure 4.7: Residuals for a hemispherical probe simulation sequence.

molecular oxygen begins to form at 4000 K. Despite oxygen displaying a faster dynamics, its later recombination prevents the mole fraction from reaching equilibrium. In contrast, nitrogen approaches a fraction which is closer to its equilibrium state because temperatures on the stagnation line reach its recombination threshold much earlier, compensating for its slower reaction kinetics. Comparing the small radius 4 mm to the hemispherical capsule with radius 25 mm some observations are to be made. While nitrogen fractions are more than 5 times higher, when the radius quadruples, oxygen fractions increase only by approximately 10% when approaching the wall. Moreover, while nitrogen drops almost monotonically with temperature, atomic oxygen fraction rises before approaching the cooled wall. This is due to the recombination of atomic nitrogen, at first acting as a catalyst with nitrogen monoxide, forming molecular nitrogen and freeing more atomic oxygen.

Velocity gradient extrapolation

The two methods described in (2.75) and (2.87) are now used to estimate a β for every tested geometry. An example of the plots used for the extrapolation in shown in Figure 4.9. Note that the variables' names have been changed

according to the observation made in section 2.3 about body-fitted reference frames.

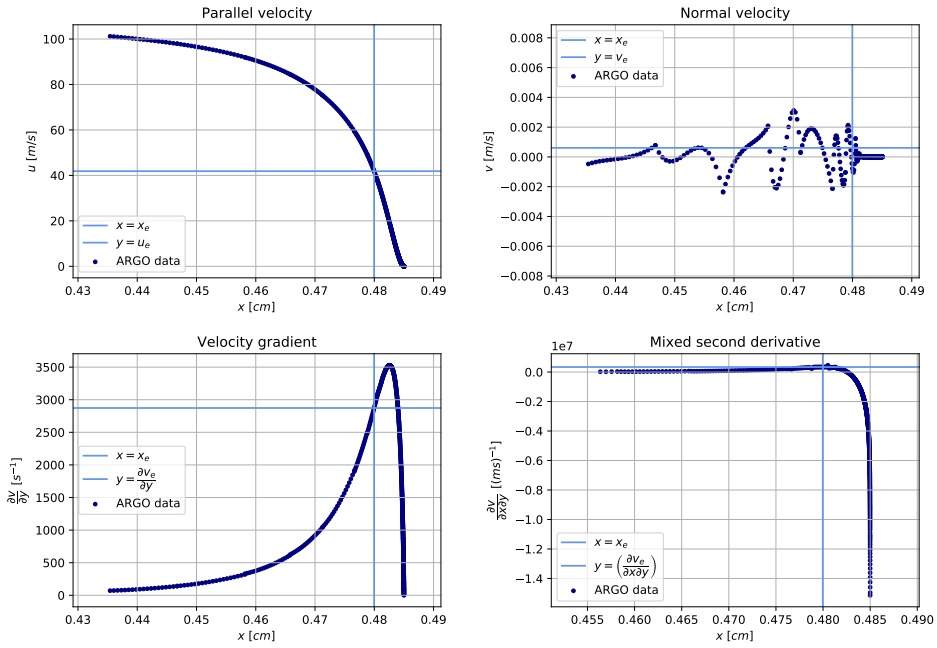

Figure 4.9: Tyipical data plots used in the β estimation procedure.

The first observation is that the normal component is affected by numerical approximations, as its value should be exactly zero on the stagnation line. This demonstrates that, even with a more careful strategy for boundary layer edge location, the procedure is not sufficiently refined. Note that the contribution of v_e in (2.87) is multiplied by the second derivative, which is non-negligible. This plot is particularly useful for illustrating the properties of the solver and the concept behind the filtering strategy. The approximation is made using third-order polynomials, and cell interfaces are recognizable by duplication of boundary values, which may exhibit jumps consistent with the description of DG methods of section 3.1. These two values are substituted with their intermediate value during post-processing via a user-implemented filter. The extrapolated β with varying R_c are shown in Figure 4.10 and summarized in Table 4.5.

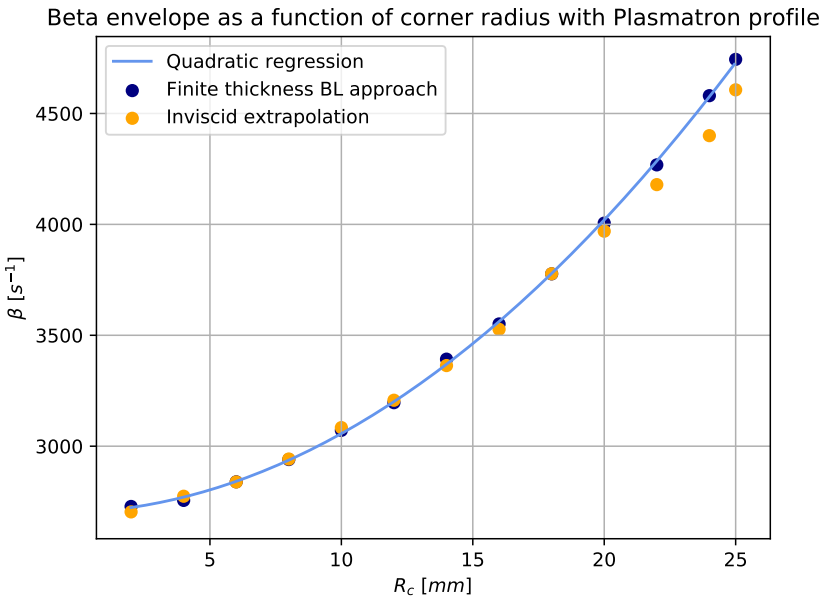

Figure 4.10: β as a function of the corner radius with a torch inlet profile.

Corner radius [mm]	$\boldsymbol{\beta_I}$ $[\boldsymbol{s^{-1}}]$	$\boldsymbol{\beta_{FT}}$ $[\boldsymbol{s^{-1}}]$
2.00	2703.74	2728.28
4.00	2774.39	2755.62
6.00	2838.71	2839.36
8.00	2942.14	2939.86
10.00	3083.89	3071.46
12.00	3207.20	3196.17
14.00	3363.53	3392.40
16.00	3526.95	3551.09
18.00	3777.37	3776.97
20.00	3969.34	4005.78
22.00	4179.28	4268.25
24.00	4400.01	4580.25
25.00	4606.56	4743.87

Table 4.5: β values for the different corner radii with a torch inlet profile.

It is clear that the finite thickness boundary layer approach is more stable and can overcome stifness issues. This can be due to the fact that linear interpolation can be severly compromised by the number of points chosen around the inflection point, possibly leading to underestimation of the linear regression slope. Even though the filter removes the singularities on the interfaces,

boundary jumps are still present. Nonetheless, the values are similar and a more careful analysis can be object of future studies to clarify the difference between the two approaches.
The general behavior seems to be parabolic with good approximation. As a result, this approach can be used for a-priori estimations of the range of β the facility is capable of inducing when varying the corner radius. From (2.74) it is possible to estimate the form of the relation between R_{eff} and R_c:

$$R_{eff} \sim (A + R_c)^{-2}, \tag{4.2}$$

where $A > 0$ depends on the specific parameters involved in the functional relation $\beta(R_c)$.

4.4 Envelope

This section is dedicated to the construction of the β envelope of the facility with varying geometries and freestream conditions. The ranges will be taken from Table 4.1.

4.4.1 Radius

To compare these results to the previous sections, the inlet conditions are derived directly from the previous profile at $y = 0$, ensuring a realistic high temperature condition. With this choice the mixture mole fractions are already computed and no further analysis on the thermodynamic state is required. The boundary conditions are

$$T_\infty = 10278.4\ K, \quad \mathbf{u}_\infty = [167.247,\ 0.000]\ \frac{m}{s}, \quad p_\infty = 100\ mbar.$$

The inclusion of a sharp corner ($R_c = 0$) completes the range of possible test geometries. While sharp corner capsules are generally inefficient due to increased heat loads and stress concentration, aerodynamic drag, flow separation and turbulence transition, plasma wind tunnel testing can utilize these models to study these features and evaluate the effects as worst-case scenarios. This case needs particularly prudent simulation strategies, as recirculation over the corner affects the robustness of the solver. Split steps have been integrated into the simulation sequence, and an exceptionally cautious CFL strategies have been adopted to enhance the solver stability. The results of atomic species mole fractions and temperature profiles near the stagnation point are in Figure 4.11.

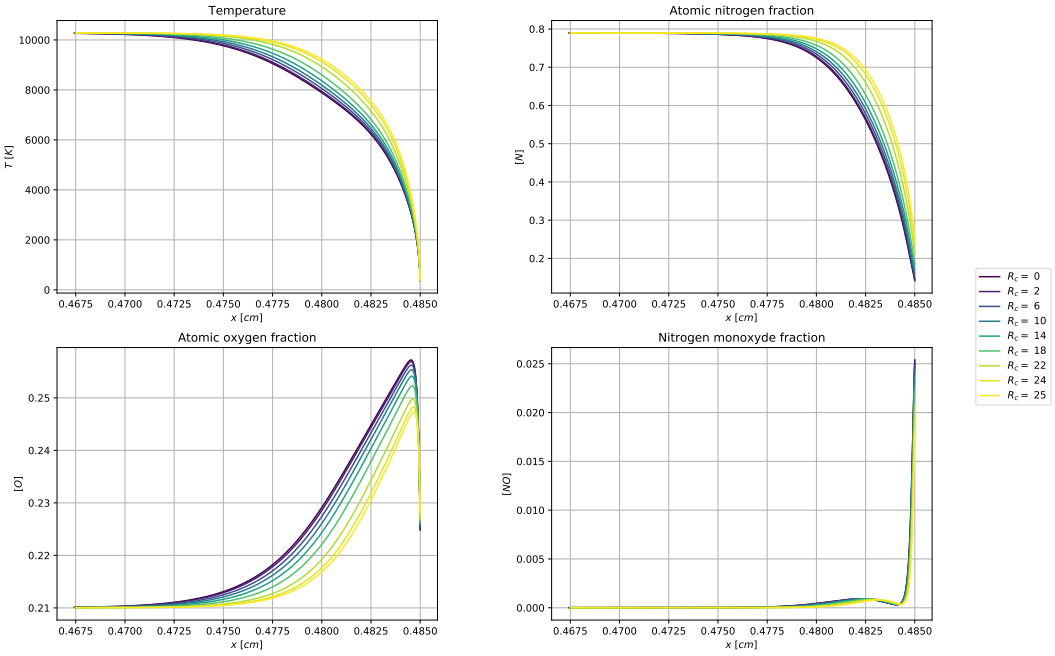

Figure 4.11: Dissociated species mole fractions and temperature along the stagnation line with different corner radii and a constant inlet.

The sharp corner case seems to align well with previous results. For the thermodynamic quantities, the same considerations of the previous sections apply, with two small differences. Due to the increased temperatures and velocities on the two-dimensional domain, partial recombination of oxygen occurs much closer to the stagnation point. With a smaller τ_{flow} atomic oxygen is unable to reach concentrations lower than the equilibrium one at $T = T_\infty$ and thus stabilizes less near the stagnation point. The same effect is visible on atomic nitrogen, which is still recombining and does not approach equilibrium. Therefore, although the general behavior is comparable to the previous sections, nonequilibrium conditions are more pronounced. The two methods described in (2.75) and (2.87) are once again used to estimate a β for every tested geometry. The effects on β is shown in Figure 4.12 and the results are summarized in Table 4.6.

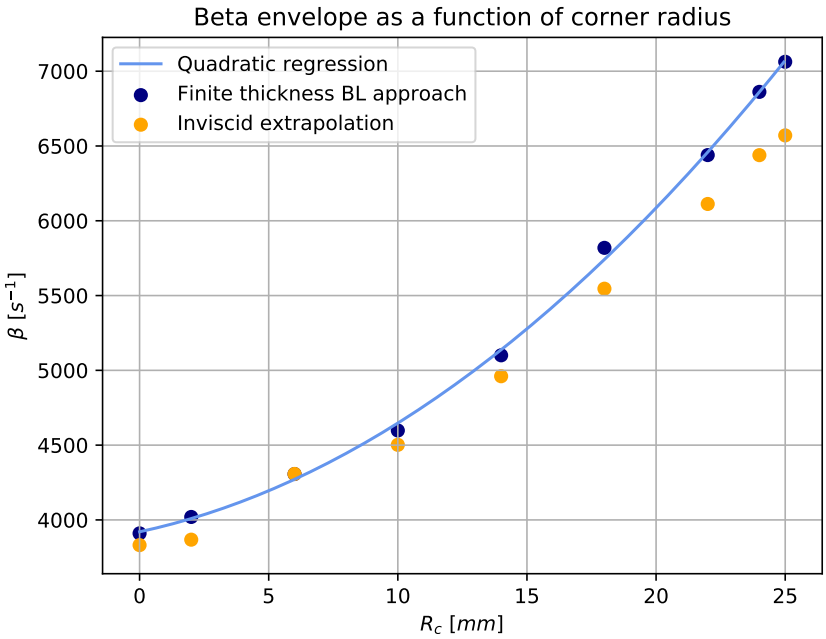

Figure 4.12: β as a function of corner radius with a constant inlet.

Corner radius [mm]	$\boldsymbol{\beta_i}$ $[\boldsymbol{s^{-1}}]$	$\boldsymbol{\beta_{FT}}$ $[\boldsymbol{s^{-1}}]$
0.00	3828.97	3907.38
2.00	3872.18	4024.07
6.00	4303.20	4298.57
10.00	4505.77	4603.20
14.00	4962.20	5101.31
18.00	5545.42	5811.50
22.00	6109.47	6436.26
24.00	6438.41	6861.48
25.00	6568.92	7060.58

Table 4.6: β values for different corner radii with a constant inlet.

These tests further prove that a finite thickness boundary layer approach is a more suitable estimation strategy. The most notable difference with Figure 4.10 is that the β parameters nearly doubled. Even though the inlet value remained unchanged along the stagnation line, low temperature zones in the domain influence the overall temperature near the stagnation point.
For the following sections the focus will be on hemispherical test probes, as they represent the most efficient shape in terms of heat load and flow separation.

4.4.2 Enthalpy

The most important parameter to tune before running a plasma wind tunnel test is the power of the high voltage generator, which will define the torch inlet enthalpy, and consequently the inlet temperature. For these first cases inlet pressure and mass flow are:

$$\dot{m} = 16 \ \frac{g}{s} \quad p_\infty = 100 \ mbar, \tag{4.3}$$

while specific enthalpies will vary in the experimental range of Table 4.1. Mole fractions and temperature along the stagnation line are in Figure 4.14.

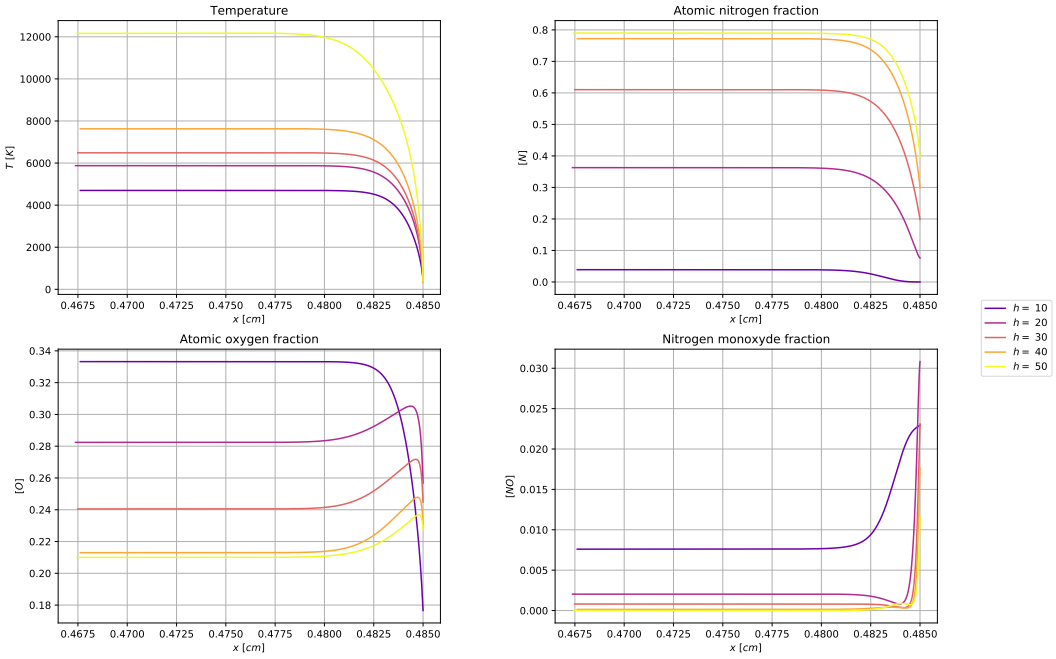

Figure 4.13: Dissociated species mole fractions and temperature along the stagnation line with different inlet specific enthalpies.

The different powers of the torch influence the inlet concentrations. A peculiar phenomenon appears for the $h = 10 \ \frac{MJ}{kg}$ case. In this scenario, the temperature is only sufficient to trigger minimal dissociation of molecular nitrogen. On the other hand, the threshold for oxygen dissociation and the formation of nitrogen monoxide is fully reached, resulting in a greater fraction of both compared to other cases with higher temperatures. Atomic oxygen monotonic recombination allows for earlier nitrogen monoxide rise, which is limited by the small fraction of atomic nitrogen available. This low-temperature case is also the only scenario where atomic nitrogen reaches equilibrium before approaching the test probe, as the dissociated fraction is already small at the inlet.

In the absence of ionization effects, the limit cases of high enthalpies, namely $h = 40\ \frac{MJ}{kg}$ and $h = 50\ \frac{MJ}{kg}$, show that the equilibrium composition of Air-5 is made approximately of 79% atomic nitrogen and 21% atomic oxygen. These percentages are the same for N_2 and O_2 in non-dissociated low-temperature air, as already seen in Figure 3.5. These two cases are also the farthest from equilibrium, since dissociated species recombination is abruptely interrupted at stagnation point. This effect is due to the higher temperatures, which, on one hand, increase the atomic nitrogen fraction in the freestream and, on the other hand, increase the velocity through the induced change in density. The result is a reduction in τ_{flow}, which lowers Da.
The envelope is shown in Figure 4.14 and the results are summarized in Table 4.7.

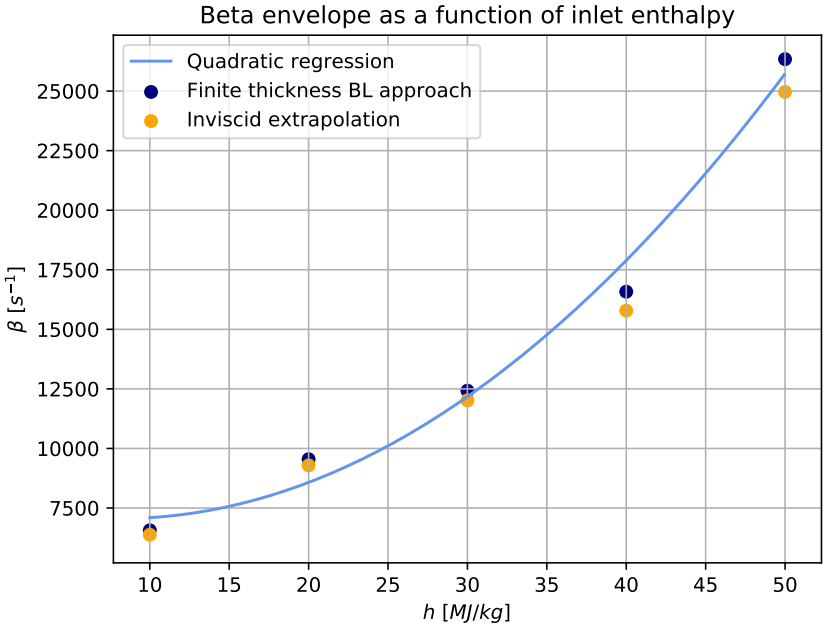

Figure 4.14: β as a function of the inlet specific anthalpy.

h [MJ/kg]	$\boldsymbol{\beta_I}$ **[s^{-1}]**	$\boldsymbol{\beta_{FT}}$ **[s^{-1}]**
10.00	6386.38	6567.49
20.00	9292.12	9551.70
30.00	12021.15	12428.94
40.00	15795.42	16584.06
50.00	24967.85	26341.80

Table 4.7: β values for different inlet specific enthalpies.

Even though the general behavior seems to be quadratic in h, the plot does not does not fit a parabola with good approximation. One reason for this result could be that enthalpy variations also trigger differences in thermodynamic and transport properties. Therefore properly evaluating and comparing the effects on the velocity gradient can becomes a difficult task. To clarify these issues, future analyses could treat this case in more detail, for instance focusing more on uncertainty quantification.

4.4.3 Pressure

The second parameter that con be controlled is the outlet pressure. For these second cases inlet enthalpy and inlet mass flow are fixed at

$$\dot{m} = 16\ \frac{g}{s}, \quad h_\infty = 25\ \frac{MJ}{kg}, \tag{4.4}$$

while pressures will vary in the experimental range of Table 4.1. Mole fractions and temperature along the stagnation line are in Figure 4.15.

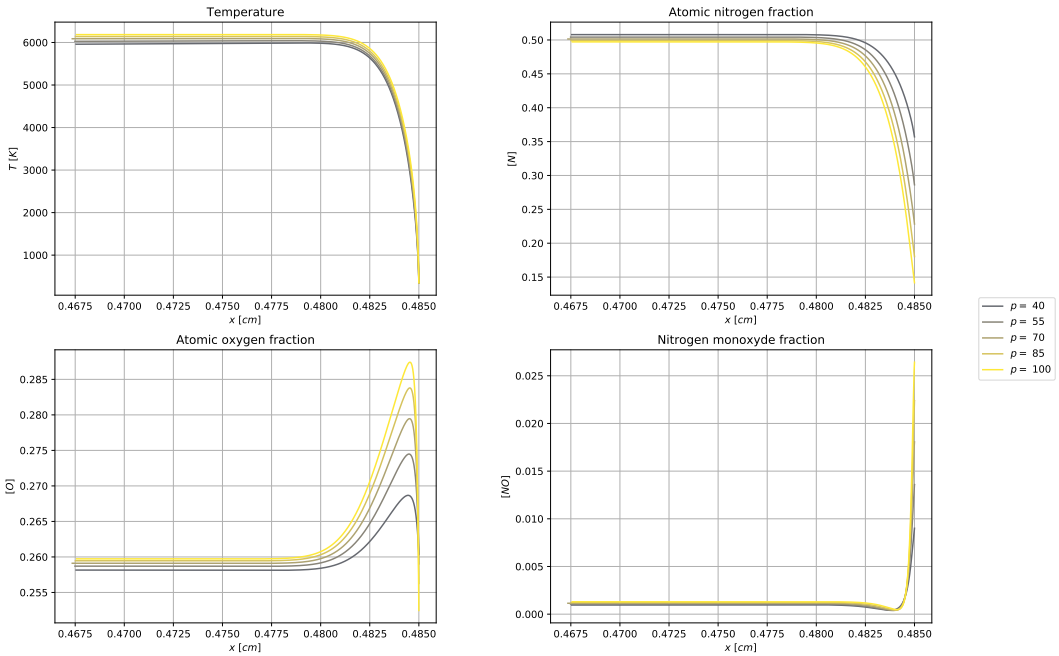

Figure 4.15: Dissociated species mole fractions and temperature along the stagnation line with different pressures.

The effects of low pressures are two-fold: they slightly alter the composition, while increasing the inlet velocity. Even though the change in the freestream composition of the mixture is almost negligible in the range considered, the

recombination near the wall is highly affectd by the added effect of low densities increasing the inlet velocity. High speeds reduce the flow time and accentuate finite rate chemistry effects, as Da decreases. However, this configuration is not rapid enough to allow a frozen mixture assumptions, as nonequilibrium effects are still visible. Atomic nitrogen fractions do not approach equilibrium before the wall, while higher dissociation levels of oxygen occur at greater pressures.
The envelope is shown in Figure 4.16 and the results are summarized in Table 4.8.

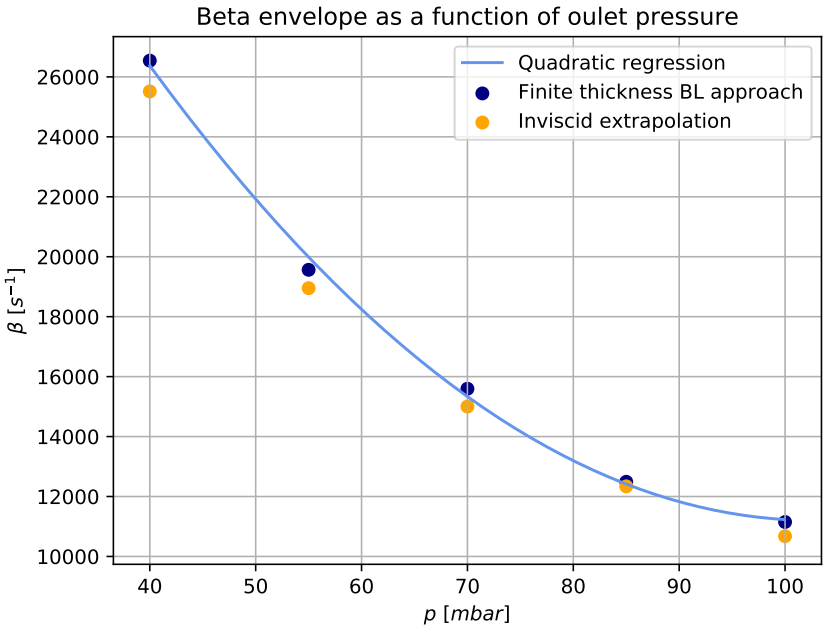

Figure 4.16: β as a function of pressure.

p [mbar]	$\boldsymbol{\beta_I}$ $[\boldsymbol{s^{-1}}]$	$\boldsymbol{\beta_{FT}}$ $[\boldsymbol{s^{-1}}]$
40.00	10681.33	11155.19
55.00	12341.38	12506.82
70.00	15003.89	15567.69
85.00	18951.01	19564.64
100.00	25519.83	26553.85

Table 4.8: β values for the different pressures.

The effects of outlet pressures seems more predictable than enthalpies. The effect is quadratic, showing strong agreement with CFD data analysis, even

without uncertainty quantification. The inviscid extrapolation appears to follow a similar pattern despite the theoretical and numerical limitations of this approach. For future experimental studies based on this treatment, this parameter appears to have a stable influence on the outcome.

4.4.4 Mass flow

The third control parameter for plasma wind tunnel testing is the inlet mass flow, as its influence is limited to the inlet velocity of the air and does not modify the thermodynamic state of the mixture. For this last cases inlet pressure and enthalpy are fixed at

$$p_\infty = 100\ mbar, \quad h_\infty = 15\ \frac{MJ}{kg}, \tag{4.5}$$

while mass flow will vary in the experimental range of Table 4.1. Mole fractions and temperature along the stagnation line are in Figure 4.17.

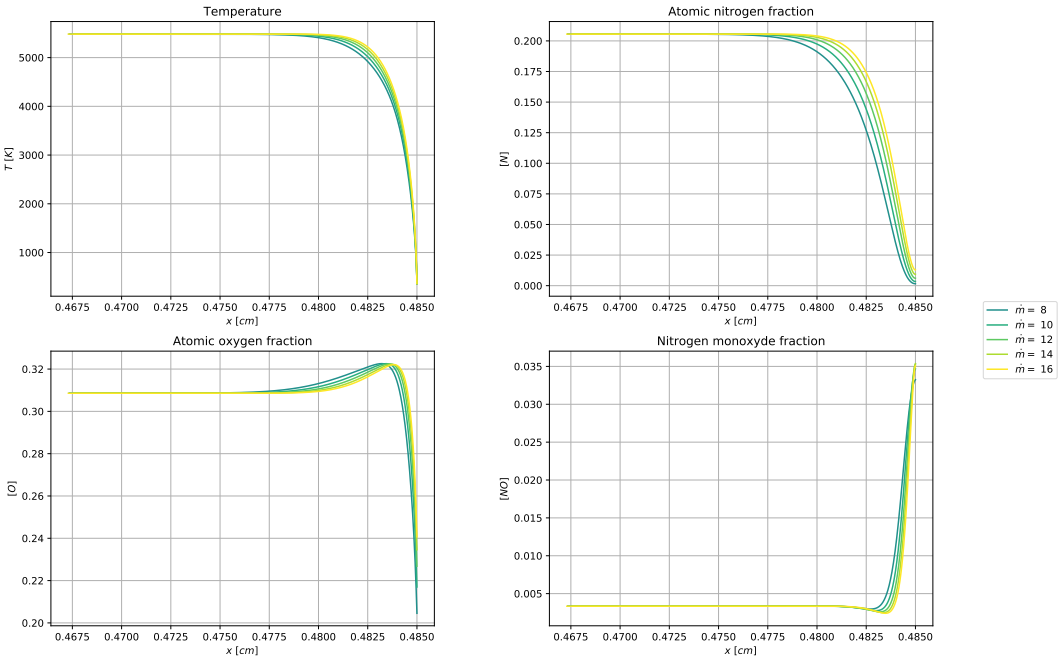

Figure 4.17: Dissociated species mole fractions and temperature along the stagnation line with different inlet mass flows.

Lower inlet mass flows result in a lower inlet velocity. The consequence is an increase in flow time, which subsequently increases the Damköhler number. This effect is evident in the nitrogen mole fraction, which is approaching equilibrium near the wall. Similarly, the oxygen mole fraction adapts more

quickly to varying conditions and drops significantly with lower mass flows. Consequently, there is a substantial increase in the monoxide fraction. The lower enthalpies used in these simulations also modify the equilibrium mixture composition, with approximately 50% of the species remaining undissociated in the freestream. The envelope is shown in Figure 4.18 and the results are summarized in Table 4.9.

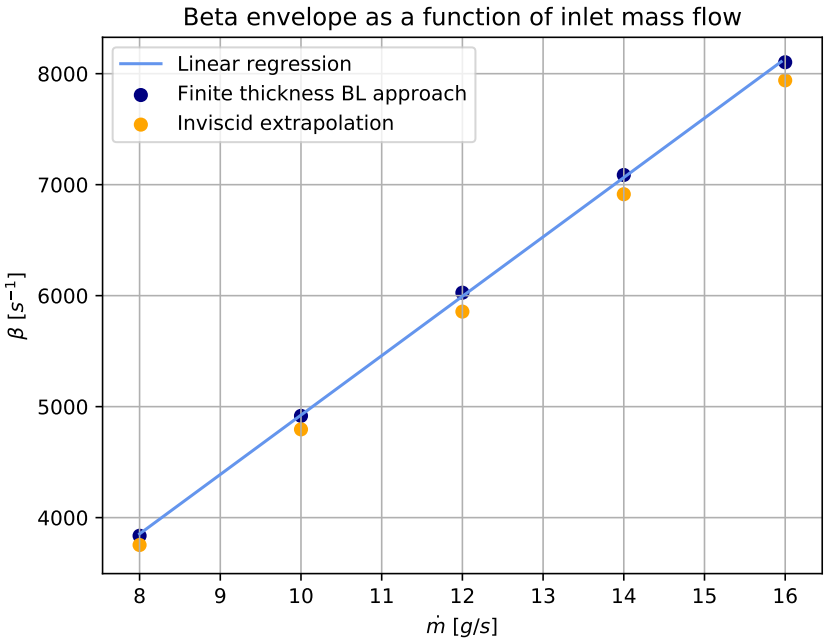

Figure 4.18: β as a function of the inlet mass flow.

p [mbar]	$\boldsymbol{\beta_I}$ $[\boldsymbol{s^{-1}}]$	$\boldsymbol{\beta_{FT}}$ $[\boldsymbol{s^{-1}}]$
8.00	3753.60	3836.18
10.00	4795.63	4916.71
12.00	5856.86	6023.09
14.00	6913.89	7089.16
16.00	7940.49	8096.62

Table 4.9: β values for the different inlet mass flows.

The effects of mass flow are undoubtedly the easiest parameter to control, as the relationship is almost certainly linear, even without rigorous uncertainty quantification on the numerical procedures. Consequently, wind tunnel tests heavily rely on this parameter to alter the physical conditions of the flow without having to carefully reconsider its consequences on the thermodynamic

state of the mixture. However, its effect is limited to flow velocity, leaving the temperature unchanged.

4.5 Flight to ground extrapolation on a real test case

For the last part of this thesis an hypersonic simulations computed with the softwaree US3D will be analyzed, in order to determine whether this particular flight condition can be reproduced into the Plasmatron facility. The numerical study is performed on an ARD capsule with a nose radius of $R = 3.36\ m$ flying at $Ma_\infty = 23.74$ at an altitude of 66.27 km. The results along the stagnation line are shown in Figure 4.19.

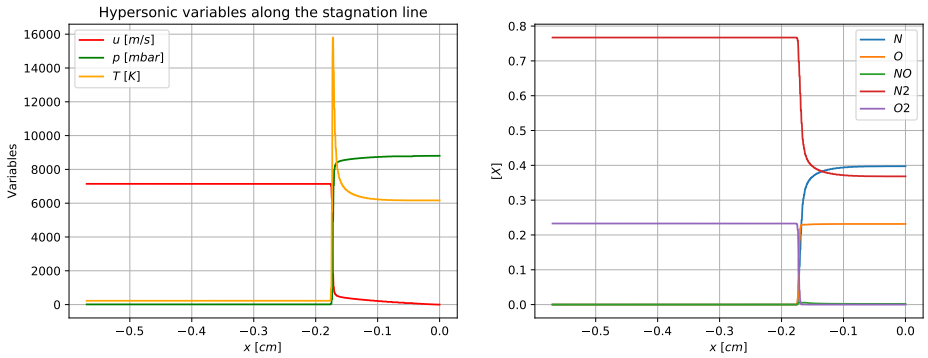

Figure 4.19: Hypersonic variables along the stagnation line.

The β can be computed analytically with (2.72):

$$\beta_{MNT} = 713.46\ s^{-1}. \tag{4.6}$$

Using equations (2.67) the equivalent subsonic freestream conditions can be extracted with the help of Mutation++. The results are

$$h_{\infty,s} = 25.53\ \frac{MJ}{kg}, \quad p_{o,s} = 90.98\ mbar. \tag{4.7}$$

Using these two conditions the strategy is to run the extreme cases of $R_c = \{0, 25\}\ mm$ and $\dot{m} = \{8, 16\}\ g/s$ and see if the β range includes the hypersonic one. The four computed β are in Table 4.10.
Based on the values of R_c and $\dot{m}$ as the only adjustable parameters within the specified range shown in Table 4.1, it appears that the flight environment being studied is not reproducible using the VKI Plasmatron facility. The extrapolated range suggests that, regardless of adjustments to the equivalent sphere

	$\boldsymbol{R_c = 0}$ mm	$\boldsymbol{R_c = 25}$ mm
$\boldsymbol{\dot{m} = 8}$ g/s	2913.61	5681.45
$\boldsymbol{\dot{m} = 16}$ g/s	5646.13	12104.09

Table 4.10: β values for different corner radii and different mass flow with fixed inlet enthalpy and pressure.

radius configuration and the mass flow, the facility does not provide a consistent replication of the intended flight conditions and thus an experimental test to infer whether the model would burn up would be conclusive. It is crucial to note that the numerical results found in this work do not represent the limits of the facility, as only a small number of parameters have been varied. To extend the study, one possibility could be to include changes in R_b. An additional case has been added with $R_b = 50$ mm, $R_c = 0$ mm, and $\dot{m} = 8$ g/s. The resulting velocity gradient is

$$\beta = 1407.18 \text{ s}^{-1}, \tag{4.8}$$

which is still not sufficient to replicate the hypersonic regime stagnation point heat load in the Plasmatron. The comparison of Figures 4.12 and 4.10 highlights a significant difference in the β parameter induced by the different boundary conditions. This discrepancy suggests that further efforts to incorporate the real profiles would greatly enhance the applicability of this strategy.

Chapter 5

Conclusions

The present work has investigated the effects of different plasma wind tunnel experimental configurations on the velocity gradient β in order to leverage information on the tested probe's response in an equivalent flight regime. The approach is based on the reactive compressible Navier-Stokes equations, incorporating high temperature effects by modeling air as a five-species mixture of thermally perfect gases with varying thermodynamic and transport properties, which are computed with Mutation^{++}. The library is coupled to the CFD solver ARGO, which uses a high order DG discretization, combinining the advantages of both FEM and FVM.

The composition of the mixture at the inlet is primarily determined by the generator's power, which sets the specific enthalpy and thus the temperature, as pressures in the range of Table 4.1 don't affect it substantially. Recombination near the wall exhibits different behaviors depending on the Dämkohler number, which varies with inlet velocity. Inlet velocity is influenced by all of the thermodynamic variables: low pressures, high enhalpies and high mass flows reduce the characteristic time of the flow, resulting in delayed chemical reactions. However, the limits of frozen and equilibrium composition are never attained near stagnation point.

Each variation has demonstrated a precise effect on the parameter β. In particular, a quadratic influence emerges from changes in corner radii, enthalpy, and pressure, while β increases linearly with mass flow, as shown in Figures 4.12, 4.14, 4.16 and 4.18. Even though the general behavior of the varying corner radius is the same with a constant and non-constant inlet, the Plasmatron test case has shown the importance of including realistic inlet profiles in the pre-processing phase, necessitating more careful meshing strategies. Moreover, the differences in β induced by a torch profile and a constant inlet are significant, and cannot be ignored.

A hypersonic simulation was conducted to assess whether the VKI Plasmatron facility can replicate the corresponding flight's peak heat load. The results

clearly showed that, with the computational model and parameters included in this study, it would not be appropriate to test a component expected to fly in those conditions in the Plasmatron facility, as the parameter β cannot be reached within the experimental range in Table 4.1. However, a more accurate analysis involving additional parameters and realistic torch profiles could demonstrate the facility's ability to replicate the hypersonic flight conditions presented in Figure 4.19, given the difference in β induced by freestream boundary conditions.
Paying attention to the extrapolation methods, the inviscid approach appears to be stable under varying physical conditions but less so with varying corner radii compared to the finite thickness approach. This is partly due to the inviscid extrapolation relying on linear regression, which is influenced by the geometric configuration of the probe. A fixed hemispherical geometry smoothly diverts the flow, whereas sharp corners can induce recirculation. It is worth noting that the former approach generally results in a slight undervaluation of the β parameters, suggesting either that the inviscid velocity gradient grows more than linearly in the boundary layer region, or that the slope of the linear regression is consistently underestimated in the numerical extrapolation procedure.

5.1 Perspectives

Further studies could improve the accuracy of this work by considering realistic inlet profiles, as well as additional effects on the β parameter such as radiation energy balance and electromagnetic interactions by varying the distance from sample holder to the torch. The construction of a more comprehensive and realistic envelope, incorporating all possible physical and geometric effects on β, can be achieved by extending the codes developed for the present work. A multivariate regression could then be used to extrapolate a precise configuration of both the Plasmatron wind tunnel physical conditions and the geometry of the test probe from a given flight environment, potentially simplifying the test engineer's work.
Although the numerical procedure presented in this work is sufficient for a preliminary study, the β extrapolation methods are unfavourable for a DG solver. More robust procedures could enhance the quality of the results by exploiting the richness of DG methods without relying on inflection point searching algorithms, thereby avoiding unnecessary accuracy losses. Nevertheless, the most beneficial contribution for a more comprehensive treatment would be a study on uncertainty quantification in the numerical extrapolation. This can significantly benefit the quality of the results, allowing future test engineers to rely on a more solid foundation.

Bibliography

[1] J. M. Bouilly et al. "Ablative thermal protection systems for entry in Mars atmosphere. A presentation of materials solutions and testing capabilities". In: *4th International Planetary Probe Workshop, Pasadena California* (2006).

[2] S. Solomon et al. "Irreversible climate change due to carbon dioxide emissions". In: *Proceedings of the National Academy of Sciences of the United States of America* (2009).

[3] Turchi A. et al. "Duplication of hypersonic stagnation-region aerothermochemistry and gas-surface interaction in high-enthalpy ground testing". In: *Experiments in Fluids* 62.10 (2021). DOI: 10.1007/s00348-021-03320-6.

[4] John D. Anderson. *Hypersonic and high temperature gas dynamics*. AIAA Educational Series, 1989. ISBN: 978-1624105142.

[5] John D. Anderson. *Modern Compressible Flow: With Historical Perspective*. McGraw-Hill Education, 2021. ISBN: 978-1260471441.

[6] Jr. Anderson John D. *Fundamentals of Aerodynamics*. 6th. McGraw-Hill Education, 2016.

[7] D. N. Arnold et al. "Unified analysis of discontinuous Galerkin methods for elliptic problems". In: *SIAM Journal on Numerical Analysis* 39.5 (2001), pp. 1749–1779.

[8] P. Barbante and O. Chazot. "Flight Extrapolation of Plasma Wind Tunnel Stagnation Region Flowfield". In: *Journal of Thermophysics and Heat Transfer* 20 (2006), pp. 493–499. DOI: 10.2514/1.17185.

[9] P. F. Barbante. "Heat Flux Duplication Between Ground Facility and Hypersonic Flight". In: *Journal of Thermophysics and Heat Transfer* 23.4 (2009), pp. 684–692. DOI: 10.2514/1.35808.

[10] P. F. Barbante and T.E.Magin. *Fundamentals of hypersonic flight-Properties of high temperature gases*. NATO STO, RTO-EN-AVT-116. May 2004.

[11] P.F. Barbante. "Accurate and efficient modelling of high temperature nonequilibrium air flows". PhD thesis. Universite Libre de Bruxelles, VKI, May 2001.

[12] F. Bassi and S. Rebay. "A High-Order Accurate Discontinuous Finite Element Method for the Numerical Solution of the Compressible Navier–Stokes Equations". In: *Journal of Computational Physics* 138.2 (1997), pp. 251–276. DOI: 10.1006/jcph.1997.5776.

[13] J. C. Boison and A. C. Curtiss. "An Experimental Investigation of Blunt Body Stagnation Point Velocity Gradient". In: *ARS Journal* 29.2 (1959), pp. 130–135.

[14] Michael J. Zehe Bonnie J. McBride and Sanford Gordon. *NASA Glenn Coefficients for Calculating Thermodynamic Properties of Individual Species*. Tech. rep. NASA/TP—2002-211556, 2002.

[15] B. Bottin. *Computation of thermodynamics properties of arbitrary perfect gas mixture at low pressures and high temperatures*. Tech. rep. 195, Von Karman Institute for Fluid Dynamics, 1997.

[16] Benoit Bottin et al. "The VKI Plasmatron Characteristics and Performance". In: (Apr. 2000), p. 26.

[17] J. H. Lienhard IV C. L. Tien. *Statistical Thermodynamics*. Holt Rinehart and Winston, 1971.

[18] Corentin Carton de Wiart. "Towards a discontinuous Galerkin solver for scale-resolving simulations of moderate Reynolds number flows, and application to industrial cases". PhD thesis. May 2014.

[19] O. CHazot. "Seminars in Hypersonic". Lectures at von Kàrman Institute for Fluid dynamics.

[20] B. Cockburn. "Discontinuous Galerkin methods". In: *Journal of Applied Mathematics and Mechanics* (2003).

[21] R. T Davis. "Numerical solution of the hypersonic viscous shock-layer equations". In: *AIAA Journal* (1970).

[22] R. T. Davis. "Second-order boundary-layer effects in hypersonic flow past axisymmetric blunt bodies". In: *Journal of Fluid Mechanics* (1964), pp. 593 –623.

[23] S. R. De Groot and P. Mazur. *Non-Equilibrium Thermodynamics*. Dover Books on Physics. Dover Publications, 1984. ISBN: 978-0486647418.

[24] Milton Dyke. "Higher-Order Boundary-Layer Theory". In: *Annual Review of Fluid Mechanics* 1 (Nov. 2003), pp. 265–292. DOI: 10.1146/annurev.fl.01.010169.001405.

[25] J. A. Fay and F. R. Riddell. "Theory of Stagnation Point Heat Transfer in Dissociated Air". In: *Journal of the Aeronautical Sciences* 25.2 (Feb. 1958).

[26] J.H. Ferziger and H.G. Kaper. *Mathematical Theory of Transport Processes in Gases*. Amsterdam, London: North-Holland Publishing Company, 1972.

[27] D. G. Fletcher. *Fundamentals of hypersonic flow-Aerothermodynamics*. NATO STO, RTO-EN-AVT-116. May 2004.

[28] G.J. Gassner and David A. Kopriva. "A comparison of the dispersion and dissipation errors of Gauss and Gauss-Lobatto discontinuous Galerkin spectral element methods". In: *SIAM Journal on Scientific Computing* 33.5 (2011), pp. 2560–2579.

[29] Vincent Giovangigli. *Multicomponent Flow Modeling*. Modeling and Simulation in Science, Engineering and Technology. Birkhauser, 1999. ISBN: 978-0817640481.

[30] Gupta R.N. et al. Gnoffo P.A. *Conservation equations and physical models for hypersonic airflows in thermal and chemical nonequilibrium*. Tech. rep. TP-2867, NASA, 1989.

[31] R. Goulard. "On Catalytic Recombination Rates in Hypersonic Stagnation Heat Transfer". In: *Journal of Jet Propulsion* 28.11 (1958), pp. 737–745. DOI: 10.2514/8.7444.

[32] Koen Hillewaert. "Devlopment of the discontinuous Galerking method for high-resolution, large scale CFD and acoustics in industrial geometries". PhD thesis. Universite Libre de Bruxelles, Feb. 2013.

[33] John T. Howe. *Hypervelocity atmospheric flight: Real gas flow fields*. Tech. rep. NASA, 1989.

[34] O. Chazot I. Şakraker A. Turchi. "Hypersonic Aerothermochemistry Duplication in Ground Plasma Facilities: A Flight-to-Ground Approach". In: *Journal of Spaccraft and Rockets* 52.5 (2015). DOI: https://doi.org/10.2514/1.A33137.

[35] Guang-Shan Jiang and Chi-Wang Shu. "On a cell entropy inequality for the discontinuous Galerkin method". In: *Mathematics of Computation* 62.206 (1994), pp. 531–538.

[36] Jr Kenneth Szltton und Randokh A. Graues. *A general stagnation-point convective heating equation for arbitrary gas mixtures*. Tech. rep. TR-R-376, NASA, 1971.

[37] Anatoly Kolesnikov. "The concept of local simulation for stagnation point heat transfer in hypersonic flows - Applications and validation". In: 2000. DOI: 10.2514/6.2000-2515.

[38] L. D. Landau and E. M. Lifshitz. *Fluid Mechanics*. Pergamon Press, 1987.

[39] Lester Lees. "Laminar Heat Transfer Over Blunt-Nosed Bodies at Hypersonic Flight Speeds". In: *Journal of Jet Propulsion* 26.4 (1956). DOI: 10.2514/3.4543.

[40] Meng-Sing Liou. "A sequel to AUSM, part II: AUSM+-up for all speeds". In: *Journal of Computational Physics* 214 (2006), pp. 137–170.

[41] Y. Lv and M. Ihme. "Discontinuous Galerkin method for multicomponent chemically reacting flows and combustion". In: *Journal of Computational Physics* 270 (2014), pp. 105–137.

[42] Thierry Magin. "A model for inductive plasma wind tunnels". PhD thesis. Université Libre de Bruxelles, 2004.

[43] Fernando Miró Miró. "Numerical Investigation of Hypersonic Boundary-Layer Stability and Transition in the presence of Ablation Phenomena". PhD thesis. Universite Libre de Bruxelles-VKI, Apr. 2020.

[44] Stanley Osher. "Riemann solvers, the entropy condition, and difference approximations". In: *SIAM Journal on Numerical Analysis* 21 (1984), pp. 217–235.

[45] J. Keller P. ATkins J. de Paula. *Physical Chemistry*. Oxford University Press, 2018.

[46] C. Park. *Non-Equilibrium Hypersonic Aerodynamics*. John Wiley and sons, New York, 1990.

[47] Thierry Poinsot and Denis Veynante. *Theoretical and Numerical Combustion*. Paris, France: Hermes Science Publications, 2005. ISBN: 978-2746639904.

[48] Neumann RD. *Experimental methods for hypersonics: Capabilities and limitations*. Tech. rep. Course note, 2nd Joint Europe-US Short Course on Hypersonic: GAMNI-SMAI and Uni. of Texas at Aus- tin, USAF Academy, Colorado springs, CO 80840, 1989.

[49] W.H. Reed and T.R. Hill. "Triangular mesh methods for the neutron transport equation". In: *Contractor Report LA-UR-73-479, Los Alamos Sci- entific Laboratory* (1973).

[50] Stark W. Rose P. "Stagnation-point heat transfer measurements in dissociated air." In: *Journal of Aeronautical Sciences 25(2):86–97* (1958). DOI: https://doi.org/10.2514/8.7519.

[51] T.G. Cowling S. Chapman. *The mathematical theory of non uniform gases*. Cambridge University Press, 1991.

[52] Pierre Schrooyen. "Numerical simulation of aerothermal flows through ablative thermal protection systems". PhD thesis. Universite catholique de Louvain-VKI, Nov. 2015.

[53] James B. Scoggins et al. "Mutation++: MUlticomponent Thermodynamic And Transport properties for IONized gases in C++". In: *SoftwareX* 12 (July 2020). ISSN: 2352-7110. DOI: 10.1016/j.softx.2020.100575.

[54] T. Tolker-Nielsen. *EXOMARS 2016 - Schiaparelli Anomaly Inquiry*. Tech. rep. ESA, 2017.

[55] Walter G. Vincenti and Charles H. Kruger. *Introduction to Physical Gas Dynamics*. Wiley, 1994. ISBN: 978-0471908357.

[56] Ken Norris William J. Sutherland1. "Behavioural models of population growth rates: implications for conservation and prediction". In: *Philosophical Transactions of the Royal Society of London* (2003).

[57] Z. Jiang Y. Liu. "Concept of non-ablative thermal protection system for hypersonic vehicles". In: *AIAA Journal* (2013).

[58] W. et al. Zhang. "A review of the mathematical modeling of equilibrium and nonequilibrium hypersonic flows". In: *Advances in Aerodynamics* 4 (2022). DOI: 10.1186/s42774-022-00125-x.